

Advances in experimental aeroacoustics

**Ganesh Raman^{1*}, Rakesh Chandran Ramachandran¹, K. Srinivasan²
and Robert Dougherty³**

¹Department of Mechanical, Materials, and Aerospace Engineering
Illinois Institute of Technology, Chicago IL 60616, USA

²Department of Mechanical Engineering, Indian Institute of Technology Madras,
Chennai 600036, India

³OptiNav Inc., USA

A review of modern experimental methods in aeroacoustics is provided along with sample applications. Specific emphasis has been placed on four advanced experimental techniques: (i) beamforming, (ii) acoustic holography, (iii) phase averaging and simultaneous flow/acoustic measurements and (iv) higher order spectral analysis. Through a description and analysis of recent successful application scenarios of the above techniques, their immense potential in experimental aeroacoustics is highlighted.

Contents

Dedication

1. Introduction

2. Microphone Array Beamforming

2.1 Methodology

2.1.1 Conventional Beamforming

2.1.2 DAMAS Inverse Problem

2.1.2.1 DAMAS2

2.1.3 CLEAN-SC

2.1.4 Orthogonal Beamforming

2.1.5 Generalized Inverse Beamforming

2.2 Experimental Validation of Acoustic Phased Array

2.2.1 Jet Noise Localization using Phased Microphone Array

2.2.2 Wind Turbine Noise Localization Using a Compact Microphone Array

2.2.3 Phased Array Experiments on Detecting Flow Separation

2.2.4 Detecting Air Leakage in Buildings Using Microphone Array and Beamforming

3. Acoustic Holography

3.1. Introduction

3.2. Implementation of NAH in Wind Tunnel

4. Simultaneous Flow/Acoustic Measurements

4.1. Phase averaged measurement technique

4.2. Two point measurement technique

5. Higher Order Spectral Analysis

5.1. Introduction

5.2. Principle

5.3. Implementation

6. Conclusions

Acknowledgments

References

^{1*}Deputy Vice-Provost for Research, Email: Raman@iit.edu

Prof. Y. Sakakibara served as the sole independent editor for this paper

NOMENCLATURE

X	-	pressure signal from the microphones
U	-	uniform velocity of the flow
$\sigma(t)$	-	emitted signal
$\delta()$	-	kroncker delta
Δt_e	-	time delay for the signal to travel from the source to the microphone
P	-	pressure vector
c	-	speed of sound
x	-	microphone coordinates
ξ	-	grid point coordinates
M	-	Mach number
β	-	$1 - M ^2$
e	-	the steering vector
C	-	Cross spectral matrix
f	-	frequency of interest
A	-	source auto powers
P_m	-	pressure transform of microphone m
Q_j	-	source strength at grid point j
\hat{X}	-	unknown source strength
\hat{Y}	-	source strength from classical beamforming
\mathcal{J}	-	total number of source points
ϑ	-	successive under relaxation parameter
w_j	-	weight vectors
D	-	degraded Cross Spectral Matrix
ϕ	-	loop gain
Λ	-	diagonal matrix of eigenvalues
V	-	orthonormal eigenvector matrix
K_i	-	characteristic signal form at the i^{th} transducer location

DEDICATION

This review article on advances in experimental aeroacoustics is a tribute to the life of Prof. Junjiro Iwamoto who made important contributions to the understanding of impinging jets and the Hartmann resonator. Two of the authors (G. Raman and K. Srinivasan) interacted with Prof. Iwamoto who also served on the editorial board of the International Journal of Aeroacoustics. The authors hope that in addition to keeping Prof. Iwamoto's memory alive, this article will serve as a resource for those working in the area of experimental aeroacoustics.

1. INTRODUCTION

Classical and modern experimental techniques in aeroacoustics are resplendent in various resources in the literature ([1–5]). Therefore, the objective of this review is to collate in a single source only the recent advances made in the leading edge areas of experimental aeroacoustics. The need for this paper arose from the fact that advanced experimental techniques in aeroacoustics have emerged from diverse areas – ranging from turbo machinery noise to free-jet noise. We believe that an amalgamation of these fertile techniques would significantly advance the state of the art in experimental aeroacoustics. Four specific techniques have been highlighted: (i) beamforming, (ii) acoustic holography, (iii) simultaneous flow/acoustic measurements and (iv) higher order spectral analysis. This paper briefly explains the principle of these four specific techniques and suitable examples of applications are provided.

2. MICROPHONE ARRAY BEAMFORMING

From the first application of phased array beamforming in aeroacoustics [6], the conventional, frequency-domain, beamforming algorithm has been the baseline method for benchmarking advanced algorithms. For a conceptual understanding of beamforming, it is convenient to begin with the time-domain version, “delay and sum,” but it is seldom actually used in aeroacoustics. The reason for the preference for the frequency-domain formulation may be that the dependence of the source on frequency and space is usually the main objective of the investigation. One place where the time-domain method is appropriate is when coherent tracking of rotating blades are required, as in the treatment of wind turbines in Europe.

Results from the conventional beamforming method have two shortcomings that limit their usefulness: spatial resolution and sidelobes. The importance of resolution is intuitively clear. Sidelobes can have two detrimental effects: if the decibel scale and the field of view of the color contour beamform map are set so that the sidelobes are visible, then users can be misled. Decreasing the dynamic range of the plot or cropping it in space to hide the sidelobes can also conceal the true sources.

In the last decade, deconvolution algorithms from photographic image processing and radio astronomy have been applied and extended to improve the resolution and sidelobes in aeroacoustics. Boone et al. [7] and Dougherty and Stoker [8] applied CLEAN. Brooks and Humphreys [9] got the attention of the community with a deconvolution algorithm for mapping acoustic sources (DAMAS). Dougherty made DAMAS more practical by improving its speed as DAMAS2 [10]. Sijtsma improved CLEAN for aeroacoustics applications by providing CLEAN-SC [11]. Dougherty applied cross-correlation beamforming by itself [12]. Dougherty and Podboy [13] used a CLEAN-like deconvolution called TIDY to generate wideband results. Sarradj [14] has emphasized a signal subspace approach called Orthogonal Beamforming.

2.1. METHODOLOGY

2.1.1. Conventional beamforming

Figure 1 shows the typical arrangement of a microphone array facing a noise source. The first step is to assume a scanning grid plane with a specific number of grid points (ξ). The pressure signals at the microphone locations will then satisfy the convective wave equation (Eq. 1),

$$\nabla^2 X - \frac{1}{c^2} \frac{\partial^2 X}{\partial t^2} + \vec{U} \cdot \nabla X = \sigma(t) \delta(\vec{x} - \vec{\xi}) \quad (1)$$

Here X is the pressure signal from the microphones, U is the uniform velocity of the flow and $\sigma(t)$ is the emitted signal. A free space Green’s function solution for Eq. 1 is given by Eq. 2,

$$X = \frac{-\sigma(t - \Delta t_e)}{4\pi \sqrt{\left(\vec{M} \cdot (\vec{x} - \vec{\xi}) + \beta^2 \|\vec{x} - \vec{\xi}\|^2 \right)}} \quad (2)$$

Here \vec{M} is the vector Mach number of the flow (\vec{U}/c) and $\beta = 1 - \|\vec{M}\|^2$. The time delay for the signal to travel from the source to the microphone is given by Δt_e in Eq. 3,

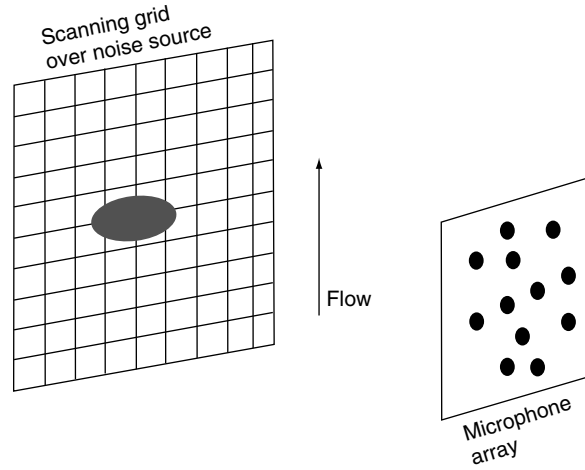


Figure 1: Microphone array layout.

$$\Delta t_e = \frac{1}{c\beta^2} \left(-\vec{M} \cdot (\vec{x} - \vec{\xi}) + \sqrt{\left(\vec{M} \cdot (\vec{x} - \vec{\xi}) + \beta^2 \|\vec{x} - \vec{\xi}\|^2 \right)} \right) \quad (3)$$

Now the actual signal emitted from the source can be approximated in time domain using Delay and Sum technique. To perform this reconstruction, we introduce $\tau = t - \Delta t_e$, find $\sigma_n(\tau)$ for each microphone signal and sum them up for N microphones (see Eq. 4) to obtain the source signal at a particular grid point (ξ_j).

$$\square(\xi) = \frac{1}{N} \square_{(n=1)}^N \square_n(\xi) \quad (4)$$

Now by calculating the complex pressure amplitudes, $\hat{\sigma}$ (by performing Fast Fourier Transform (FFT)), we can obtain the source auto powers as expressed in Eq. 5,

$$A = \frac{1}{2} \left(\sum_{(n,m)}^N \left(\hat{\sigma}_n \hat{\sigma}_m^* \right) / \sum_{(n,m)}^N 1 \right) \quad (5)$$

We can then convert the auto powers into Sound Pressure Level (SPL) and plot a SPL contour map at every grid point. This is known as a ‘beamform map’. The solution given above is for the beamforming problem in time domain. One could solve the same problem in frequency domain using classical beamforming.

In the frequency domain the beamforming problem is posed as a minimization problem. The aim of this problem is to solve for complex amplitudes ‘a’ of sources in \in by computing the pressure vector \mathbf{p} with the steering vector \mathbf{e} through minimization of,

$$J = \|\mathbf{p} - \mathbf{a}\mathbf{e}\|^2 \quad (6)$$

The solution to this problem is given by Eq. 7,

$$a = \frac{\mathbf{e}^* \mathbf{p}}{\|\mathbf{e}\|^2} \quad (7)$$

We can write the above equation in terms of source auto powers

$$A = \frac{1}{2} E \left[\|a\|^2 \right] = \frac{1}{2} E \left[aa^* \right] = \frac{1}{2} E \left[\frac{e^* p p^* e}{\|e\|^4} \right] = \frac{e^* C e}{\|e\|^4} \quad (8)$$

where $E[\dots]$ represents a time average of multiple records. We can then plot the beamform map by calculating the SPL from the auto powers. Here e is the steering vector from the grid point to the microphone. This result can be obtained by taking the Fourier transform of Eq. 2,

$$p = \frac{-a \exp(-2\pi \text{ if } \Delta t_d)}{4\pi \sqrt{\left(\vec{M} \cdot (\vec{x} - \vec{\xi}) + \beta^2 \|\vec{x} - \vec{\xi}\|^2 \right)^2}} \quad (9)$$

Where 'a' is the Fourier transform of σ . From this Eq. 9 we get our steering vector as,

$$e = \frac{\exp(-2\pi \text{ if } \Delta t_e)}{4\pi \sqrt{\left(\vec{M} \cdot (\vec{x} - \vec{\xi}) + \beta^2 \|\vec{x} - \vec{\xi}\|^2 \right)^2}} \quad (10)$$

The beamform maps obtained from source auto powers (using both delay and sum and classical beamforming) will result in a considerable number of sidelobes, especially when the auto powers dominate the cross powers. A typical scenario occurs when the microphone array is on the wall of a wind tunnel. For these types of windy cases we can eliminate the auto powers to reduce the sidelobes and obtain a much cleaner map (see Eq. 11).

$$A = \frac{\sum_{(n,m)} e_n^* C_{nm} e_m}{\sum_{(n,m)} |e_n|^2 |e_m|^2} \quad (11)$$

where $\{(n,m)\}$ excludes the diagonal elements, $n=m$. To get a much cleaner beamform map, advanced deconvolution methods are necessary. The widely used deconvolution techniques in beamforming include DAMAS, DAMAS2, CLEAN-SC, and TIDY.

2.1.2. DAMAS inverse problem

A brief summary of the DAMAS inverse problem as explained by Brook et al. [9] is presented here. The inverse problem is posed such that the source strength distributions are extracted cleanly from the beamforming array characteristics. First, the pressure transform P_m of microphone m of Eq. (5) is related to a modeled compact source located at position n in the source field.

$$P_{m:j} = Q_j \cdot e_{m:j} \quad (12)$$

Here Q_j represents the source strength, normalized to the pressure at distance r_c . The product of pressure-transform terms of Eq. (5) becomes

$$P_{m:j}^* \cdot P_{m':j} = (Q_j \cdot e_{m:j})^* (Q_j \cdot e_{m':j}) = Q_j^* Q_j (e_{m:j})^* (e_{m':j}) \quad (13)$$

When this is substituted into Eq. (5), one obtains the modeled microphone array Cross Spectral Matrix (CSM) for a single source located at n

$$\hat{G}_{j\text{mod}} = X_j \begin{bmatrix} (e_1)^* e_1 & (e_1)^* e_2 & \cdots & \cdots & (e_1)^* e_{m_0} \\ (e_2)^* e_1 & (e_2)^* e_2 & & & \vdots \\ \vdots & & \ddots & & \vdots \\ \vdots & & & \ddots & \vdots \\ (e_{m_0})^* e_1 & \cdots & \cdots & \cdots & (e_{m_0})^* e_{m_0} \end{bmatrix} = X_j \hat{e} \hat{e}^T \quad (14)$$

where $X_j = 2Q_j^* Q_j / T$ is the mean square pressure per bandwidth at each microphone m normalized in level for a microphone at $r_m = r_c$. Assuming that there are N number of statistically independent sources, each at different positions 'n', a CSM is modeled:

$$\hat{G}_{\text{mod}} = \sum_j \hat{G}_{j\text{mod}} \quad (15)$$

Employing this in Eq. (11),

$$Y_{j\text{mod}}(\hat{e}) = \left[\frac{\hat{e}_j^T \hat{G}_{j\text{mod}} \hat{e}_j}{(\hat{e}_j^T \hat{e}_j)^2} \right] \quad (16)$$

Restated,

$$Y_{j\text{mod}}(\hat{e}_j) = \prod_{j \in \Omega} A_{j \in \Omega} X_{j \in \Omega} \quad (17)$$

where

$$A_{j \in \Omega} = \frac{\hat{e}_j^T \hat{e}_{j \in \Omega} \hat{e}_{j \in \Omega}^T \hat{e}_j}{(\hat{e}_j^T \hat{e}_j)^2} = \left| \frac{\hat{e}_j^T \hat{e}_{j \in \Omega}}{\hat{e}_j^T \hat{e}_j} \right|^2 \quad (18)$$

By equating $Y_{j\text{mod}}(\hat{e})$ with processed $Y(\hat{e}) = Y_j$ from measured data, we have

$$\hat{A} \hat{X} = \hat{Y} \quad (19)$$

where the matrices \hat{A} , \hat{X} , and \hat{Y} have components $A_{j \in \Omega}$, X_j and Y_j , respectively. A single linear equation component of Eq. (19) is

$$A_{j1} X_1 + A_{j2} X_2 + \dots + A_{jj} X_j + \dots + A_{j\mathcal{J}} X_{\mathcal{J}} = Y_j \quad (20a)$$

Using $A_{jj} = 1$, this is rearranged to give

$$X_j = Y_j - \left[\sum_{j'=1}^{j-1} A_{jj'} X_{j'} + \sum_{j'=j+1}^{\mathcal{J}} A_{jj'} X_{j'} \right] \quad (20b)$$

This equation is used in an iteration algorithm to obtain the source distribution X_j for all j between 1 and \mathcal{J} as per the following equations with a non negativity constraint on X :

$$\begin{aligned}
 X_1^{(i)} &= Y_1 - \left[0 + \sum_{j'=1+1}^J A_{1j'} X_{j'}^{(i-1)} \right] \\
 X_j^{(i)} &= Y_j - \left[\sum_{j'=1}^{j-1} A_{jj'} X_{j'}^{(i)} + \sum_{j'=j+1}^J A_{jj'} X_{j'}^{(i-1)} \right] \\
 X_J^{(i)} &= Y_J - \left[\sum_{j'=1}^{J-1} A_{Jj'} X_{j'}^{(i-1)} + 0 \right]
 \end{aligned} \tag{20c}$$

The direction of the loop j is reversed on alternate iterations: 1 ... J and then J ... 1. Eq. (20c) is the DAMAS inverse problem iterative solution.

2.1.2.1. DAMAS2

The evaluation of Eq. 20c is very expensive, as each iteration requires $O(\mathcal{J}^2)$ operations. A faster method can be developed by expressing Eq. 19 in the spatial frequency domain. Let Eq. 16 be rewritten as $Y_{\text{mod}}(\vec{\xi}_j) = \sum_j A(\vec{\xi}_j, \vec{\xi}_{j'}) X(\vec{\xi}_{j'})$ where $\vec{\xi}_j$ is the vector location of grid point n in the beamform map. As a function of $\vec{\xi}_j$ $A(\vec{\xi}_j, \vec{\xi}_{j'})$ is the beamform map that would occur for a single point source at $\vec{\xi}_{j'}$. The functional form of the PSF is often such that if the source point $\vec{\xi}_j$ is translated the resulting map approximately shifts without changing shape, i.e., $A(\vec{\xi}_j, \vec{\xi}_{j'} + \delta\vec{\xi}) \approx A(\vec{\xi}_j - \delta\vec{\xi}, \vec{\xi}_{j'})$.

This shift-invariance property can be summarized as $A(\vec{\xi}_j, \vec{\xi}_{j'}) = A(\vec{\xi}_j - \vec{\xi}_{j'})$. Using this assumption, Eq. 17 becomes $Y_{\text{mod}}(\vec{\xi}_j) = \sum_j A(\vec{\xi}_j - \vec{\xi}_{j'}) X(\vec{\xi}_{j'})$ which is recognized as a discrete convolution in $\vec{\xi}$ with kernel A . If A is considered to be a periodic function with the period of the beamform map (in 1, 2, or 3 dimensions), then the model can be considered a circular discrete convolution. Taking the discrete Fourier transform gives $\tilde{Y}_{\text{mod}}(\vec{k}_j) = \tilde{A}(\vec{k}_j) \tilde{X}(\vec{k}_j)$ for each discrete wavenumber. Eq. 19 can be evaluated in $O(\mathcal{J} \log \mathcal{J})$ operations by using the FFT algorithm to transform X to the spatial frequency domain ($O(\mathcal{J} \log \mathcal{J})$ operations), multiplying by the transform of the psf spatial frequency by spatial frequency ($O(\mathcal{J})$ operations), and using the FFT to transform back to the spatial domain ($O(\mathcal{J} \log \mathcal{J})$ operations). This approach is not suitable for solving Eq 19 by the Gauss-Seidel method used in DAMAS because the Fourier convolution evaluates the expression at all of the grid points at once. Jacobi iteration is applied instead. The algorithm for DAMAS2 is

1. Compute $\tilde{A}(\vec{k}_j) = \text{forward FFT}[A(\vec{\xi}_j)]$.
2. Set $a = \sum_j |A(\vec{\xi}_j)|$
3. Set solution $X_1^{(0)} = 0$.
4. Iterate
 - a. $\tilde{X}^{(i)} \leftarrow \text{forward FFT}[X^{(i)}]$.
 - b. For each \vec{k}_j , scale $\tilde{X}_k^{(i)}$ by $\exp(-k^2/(2k_c^2))$
 - c. Let $\tilde{r}(\vec{k}_j) = \tilde{A}(\vec{k}_j) \tilde{X}_k^{(i)}$ for each \vec{k}_j
 - d. $r(\vec{\xi}_j) \leftarrow \text{inverse FFT}[\tilde{r}(\vec{k}_j)]$.
 - e. $X^{(i+1)} \leftarrow X^{(i)} + \vartheta[Y - r]/a$.
 - f. Replace each negative element of $X^{(i+1)}$ by 0.

Step 4b is a regularization measure that suppresses high frequency components in the solution to produce a smooth result. The constant k_c is chosen to be on the order of the reciprocal of the spacing between grid points. The parameter ϑ is a successive under relaxation parameter chosen for convergence. A typical value might be 0.5.

DAMAS2 is used in the aerospace industry [15] and is related to the

Richardson Lucy technique from optical microscopy [16]. DAMAS2 has additional savings in computer time and memory because only a single PSF is computed and stored, versus a separate PSF for each source point in DAMAS. The assumption that the PSF is shift-invariant becomes less valid the wider the angular extent of the grid as seen from the perspective of the array. This variance with shift be viewed as a consequence of the fact that the numerical aperture of the array in the axial direction is reduced as a grid point moves away from the array axis. A non-uniform grid can be defined so that the resolution is approximately constant over the entire grid [10], extending the usefulness of DAMAS2 as well as optimizing the use of computer resources.

2.1.3. CLEAN-SC

In order to obtain properly resolved side lobes and other features, researchers created an alternative method that makes use of the fact that side lobes in a source plot are coherent with the main lobe. A brief description of the CLEAN-SC beamforming algorithm as explained by Sijtsma [11] is presented here. Source-cross powers are used here, which are defined by

$$B_{jk} = w_j^* \bar{C} w_k \quad (21)$$

Where \bar{C} is the CSM with its diagonal elements removed. The degraded source powers $P_j^{(0)}$ are calculated for the points on the scan grid using conventional beamforming.

$$P_j^{(0)} = w_j^* \bar{C} w_j = w_j^* \bar{D}^{(0)} w_j \quad (22)$$

where, w_j are weight vectors and D is the degraded CSM. This is called the dirty map. From Eq. 21, the peak source location is determined i.e; the scan point for which $P_j^{(i-1)}$ obtains its maximum value $P_{\max}^{(i-1)}$. Degraded source powers $P_j^{(i)}$ without the influence of this peak source are written as

$$P_j^{(i)} = P_j^{(i-1)} - w_j^* \bar{G}^{(i)} w_j \quad (23)$$

To find the $G^{(i)}$, it is required that the source cross powers of any scan point with the peak location are determined entirely by $G^{(i)}$. In other words

$$w_j^* \bar{D}^{(i-1)} w_{\max}^{(i)} = w_j^* \bar{G}^{(i)} w_{\max}^{(i)}, \text{ for all possible } w_j \quad (24)$$

Where $w_{\max}^{(i)}$ is the weight vector associated with $e_{\max}^{(i)}$. Eq. (23) is satisfied when

$$\bar{D}^{(i-1)} w_{\max}^{(i)} = \bar{G}^{(i)} w_{\max}^{(i)} \quad (25)$$

Eq. (23) does not have a unique solution for $G^{(i)}$, but Sijtsma constructed one by assuming $G^{(i)}$ is due to a single coherent source component $h^{(i)}$:

$$G^{(i)} = P_{\max}^{(i-1)} h^{(i)} h^{*(i)} \quad (26)$$

In other words, the dirty map is updated by subtracting a scaled PSF associated with $\xi_{\max}^{(i)}$. This PSF is replaced by a clean beam:

$$Q_j^{(i)} = P_{\max}^{(i-1)} 10^{-\lambda |\xi_j - \xi_{\max}^{(i)}|^2} \quad (27)$$

where, λ is a parameter determining the band width. Finally, a degraded CSM is defined:

$$D^{(i)} = D^{(i-1)} - P_{\max}^{(i-1)} h^{(i)} h^{*(i)} \quad (28)$$

Analogously to Eq. (21),

$$P_j^{(i)} = w_j^* \overline{D}^{(i)} w_j \quad (29)$$

After i iterations, the source plot is written as a summation of the clean beams and the remaining dirty map:

$$A_j = \prod_{i=1}^I Q_j^{(i)} + P_j^{(i)} \quad (30)$$

Sijtsma suggests a stop criterion of

$$\left\| \overline{D}^{(I+1)} \right\| \ll \left\| \overline{D}^{(I)} \right\| \quad (31)$$

Often a safety factor φ (called “loop gain”), with $0 < \varphi < 1$, is used in the CLEAN algorithms. This means that Eqs. (27) and (28) are replaced by

$$\begin{aligned} Q_j^{(i)} &= \varphi P_{\max}^{(i-1)} 10^{-\lambda |\xi_j - \xi_{\max}^{(i)}|^2} \\ D^{(i)} &= D^{(i-1)} - \varphi P_{\max}^{(i-1)} h^{(i)} h^{*(i)} \end{aligned} \quad (32)$$

2.1.4. Orthogonal beamforming

Orthogonal Beamforming (OB) is a deconvolution method that, like Multiple Signal Classification (MUSIC) [17], is based on Schmidt’s partition of \mathbb{C}^N into signal and noise subspaces using the eigenvalue decomposition of the CSM. Unlike MUSIC, the primary emphasis of OB is to determine source strengths and spectra, rather than source locations or beamform maps. (Schmidt does estimate the source strengths in a post process step from the MUSIC maps, but MUSIC may be too fragile for routine use in aeroacoustics.)

The basic principle of orthogonal beamforming is outlined in the following section. Suppose we have N microphones, M acoustic sources, and that the microphones also measure noise, \mathbf{n} . The data model for the complex array pressure \mathbf{p} is

$$\mathbf{p} = \mathbf{A}\mathbf{q} + \mathbf{n} \quad (33)$$

where \mathbf{q} is a complex M -vector of unsteady source strengths and \mathbf{A} is an $N \times M$ matrix whose columns are the steering vectors for the respective sources. Assuming the noise terms at the various microphones have equal amplitude n and are uncorrelated with each other and with the acoustic sources and using the notation $E[\]$ for the expected value, the cross spectral matrix becomes

$$\mathbf{C} = E[\mathbf{pp}'] = \mathbf{A}\mathbf{S}\mathbf{A}' + n^2\mathbf{I} \quad (34)$$

where $\mathbf{S} = E[\mathbf{qq}']$ is the CSM of the acoustic sources. The prime notation refers to the Hermitian conjugate.

The eigenvalue decomposition of the array CSM is written

$$\mathbf{C} = \mathbf{V}\mathbf{\Lambda}\mathbf{V}' \quad (35)$$

where $\mathbf{\Lambda}$ is the diagonal matrix of eigenvalues and \mathbf{V} is the orthonormal eigenvector matrix. If that the number of sources is less than the number of microphones, $M < N$, Schmidt [17] observed that $\mathbf{A}\mathbf{S}\mathbf{A}'$ is non-negative definite and rank deficient and must have (at least) $N-M$ zero eigenvalues. Adding the term $n^2\mathbf{I}$ to $\mathbf{A}\mathbf{S}\mathbf{A}'$ to give \mathbf{C} increases all of the eigenvalues by n^2 . It follows that the smallest $N-M$ eigenvalues of \mathbf{C} are all equal to n^2 .

$$\mathbf{\Lambda} = \begin{bmatrix} \Lambda_S + n^2\mathbf{I} & 0 \\ 0 & n^2\mathbf{I} \end{bmatrix} \quad (36)$$

where the diagonal $M \times M$ matrix Λ_S contains eigenvalues that relate specifically to the sources. Using some matrix manipulations, Schmidt shows that Λ_S and $\mathbf{A}'\mathbf{A}\mathbf{S}$ are similar matrices and therefore share the same eigenvalues and the same trace. If the sources are uncorrelated, then \mathbf{S} is diagonal and the elements on the diagonal are the source powers $S_{ii} = E[|q^i|^2]$. Diagonal element i of $\mathbf{A}'\mathbf{A}\mathbf{S}$ is $H_{ii}S_{ii}$ where

$$H_{ii} = \sum_{j=1}^M |a_{ij}|^2 \quad (37)$$

The equality of the traces of the similar matrices becomes

$$\sum_{i=1}^M H_{ii}S_{ii} = \sum_{i=1}^M \Lambda_{S_{ii}} \quad (38)$$

Next, a key approximation is made: it is assumed that sources can be ordered so that the terms of the sum are individually approximately equal:

$$S_{ii} \approx \frac{\Lambda_{S_{ii}}}{H_{ii}} \quad (39)$$

Sarradj [14] gives a bound on the error of this approximation derived from the Gershgorin circle theorem and states that it tends to become smaller with increasing frequency, number of microphones, source spacing, and eigenvalue spacing. He also shows that it can be small in numerical simulations.

As we apply the method, the eigenvalues $\Lambda_{S_{ii}}$ can be derived from the CSM, \mathbf{C} , together with an estimate for n^2 , which can be derived by examining the distribution of the eigenvalues to look for a nearly flat tail. Evaluation of H_{ii} in principle requires knowledge of the source location, although in the case of the free space propagation it depends mainly on the distance from the source to the array may be easy to estimate from the geometry of the test and actually difficult to estimate the beamforming step to follow. In any case, the transverse distribution of the source is also of interest. The individual sources are located by applying the conventional beamforming algorithm to the orthogonal components

of the CSM. The rank-1 structure of a component CSM

$$\mathbf{C}_i = \Lambda_{Sii} \mathbf{V}_i \mathbf{V}_i' \quad (40)$$

means that the conventional beamforming expression reduces to

$$B_i(\vec{\xi}) = \mathbf{w}'(\vec{\xi}) \mathbf{C}_i \mathbf{w}(\vec{\xi}) = \Lambda_{Sii} |\mathbf{w}'(\vec{\xi}) \mathbf{V}_i|^2 \quad (41)$$

where $\mathbf{w}(\vec{\xi})$ is the beamforming weight vector for the map point $\vec{\xi}$. This is a 1D sum, which is faster to evaluate than the 2D sum of full beamforming. (Sarradj offers a modified, formula for the case of diagonal deletion beamforming, although its utility is unclear since microphone self noise handled by the treatment of n^2 and only the peak location of each component beamform map is needed.)

The complete orthogonal beamforming algorithm is

1. Measure the CSM, \mathbf{C}
2. Evaluate the eigenvalue decomposition of \mathbf{C}
3. Examine the trend of the eigenvalues to estimate M and n^2
4. Initialize the total beamform map to 0
5. For each $i \in \{1..m\}$
 - a. Compute the orthogonal component beamform map using \mathbf{V}_i
 - b. Identify the peak location of the component map
 - c. Add Λ_{Sii} to the corresponding point in the total beamform map

In practice in aeroacoustics, the assumption that there are exactly $M < N$ distinct sources is a bit of an abstraction. It is not found that there are $N - M$ equal eigenvalues at the end of the list of eigenvalues listed in descending order. This makes the determination of M and n^2 somewhat difficult. Sarradj states that experiments indicate that, except for computer time no harm develops if we choose an arbitrary, somewhat large, value for M . Several aspects of the algorithm put a premium on the use of an array with a large number of microphones.

2.1.5. Generalized inverse beamforming

The beamforming techniques are designed for locating point sources. An extended, coherent source is likely to be missed altogether or located incorrectly when the extended coherent source has a directivity pattern that varies across the array. The generalized inverse method proposed by Suzuki [18] explicitly handles coherent sources. Dougherty [19] suggested an improved method which addresses the point for extended sources. The general scheme is depicted in Fig. 2. The complex vectors can be defined as follows: \mathbf{p} is the acoustic pressure at the array (N microphones), $\mathbf{p}_{\text{far field}}$ is the acoustic pressure at far field points, \mathbf{A} is the source strength at the M in-jet points, and \mathbf{s} is the alternate model of the source strength. The complex matrices \mathbf{G} and \mathbf{H} represent propagation factors between the source points and observation locations. The $(M \times M)$ matrix \mathbf{L} represents a mapping between \mathbf{s} and \mathbf{A} . The purpose of \mathbf{L} and \mathbf{s} is to alter the metric used in the linear algebra solution for the source to favor distributions that are viewed as physically reasonable. Corresponding to the acoustic vectors, there are cross spectral matrices $\mathbf{C} = \langle \mathbf{p} \mathbf{p}' \rangle$, $\mathbf{C}_{\text{far field}} = \langle \mathbf{p}_{\text{far field}} \mathbf{p}_{\text{far field}}' \rangle$, $\mathbf{C}_A = \langle \mathbf{A} \mathbf{A}' \rangle$ and $\mathbf{C}_s = \langle \mathbf{s} \mathbf{s}' \rangle$, where $\langle \rangle$ represents the time average and the prime notation indicates the complex conjugate transpose. Let the Moore–Penrose generalized inverse of \mathbf{G} be denoted \mathbf{G}^+ . On a block by-block basis, over slowly-varying time in the short-time Fourier transform, the least squares solution of minimum norm for \mathbf{A} is $\mathbf{A}_{\text{LSSM}} = \mathbf{G}^+ \mathbf{p}$. Taking the time average, the corresponding estimate for \mathbf{C}_A is

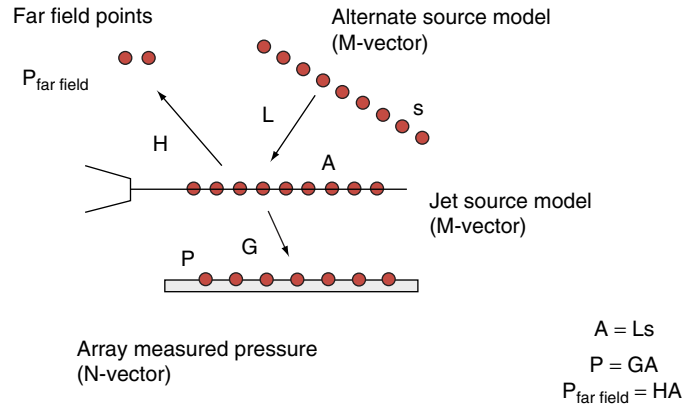


Figure 2: Acoustic quantities and matrices (reprinted from Dougherty [19], 2012 Multi-Science Publishing Co. Ltd., used with permission).

$$\mathbf{C}_{\mathbf{A}_{LSSM}} = \langle \mathbf{A}_{LSSM} \mathbf{A}'_{LSSM} \rangle = \langle \mathbf{G}^+ \mathbf{p} (\mathbf{G}^+ \mathbf{p})' \rangle = \mathbf{G}^+ \langle \mathbf{p} \mathbf{p}' \rangle \mathbf{G}^{+'} = \mathbf{G}^+ \mathbf{C} \mathbf{G}^{+'}. \quad (42)$$

By replacing the generalized inverse of \mathbf{G} (\mathbf{G}^+) with the Hermitian conjugate gives the matrix beamforming expression,

$$\mathbf{C}_{\mathbf{A}_{\text{beamforming}}} = \mathbf{G} \mathbf{C} \mathbf{G}' \quad (43)$$

We can express this using a singular value decomposition (SVD) $\mathbf{G} = \mathbf{U} \mathbf{\Sigma} \mathbf{V}'$ in Eq. 42,

$$\mathbf{C}_{\mathbf{A}_{LSSM}} = \mathbf{V} \mathbf{\Sigma}^{-1} \mathbf{U}' \mathbf{C} \mathbf{U} \mathbf{\Sigma}^{-1} \mathbf{V}' \quad (44)$$

This is the generalized inverse method solution using SVD. One needs to use regularization techniques while computing the generalized inverse. The generalized inverse technique is a powerful tool for exploiting near field arrays with extended coherent sources, such as supersonic jets.

2.2. EXPERIMENTAL VALIDATION OF ACOUSTIC PHASED ARRAY

2.2.1. Jet noise localization using phased microphone array

The application of beamforming to localize jet noise has existed for quite some time now. Several studies of jet noise using phased microphone arrays have been made (see [13] for details). Dougherty and Podboy [13] explain that many of these studies are limited to subsonic jets and have several drawbacks that prevent the structure of the jet noise source from being fully revealed. They showed that using an advanced phased array system (OptiNav Array 48) and a new deconvolution algorithm (TIDY), yields significantly more detailed results than previous jet images. A validation study was performed by Dougherty and Podboy [13] with the jet modeled as a line source with convection velocity and a coherence length. It was found that for a high frequency band (about 32 kHz OB) (a) the source region is clearly visible and (b) for successively lower bands, the apparent source extent becomes extended in the radial and then axial direction using conventional Delay-and-Sum beamforming. This was attributed to the array resolution effect (governed by Rayleigh criteria), based on the array's size and location. It was also reported that the TIDY beamforming algorithm considerably sharpens the beamforming results. Figure 3 shows the beamform maps for supersonic jet case. The array was located parallel to the jet and separated from it by 2 m. Figure 3 (a) and 3(b) show the beamform map for high frequency range (32 kHz OB) using both conventional beamforming and TIDY, respectively. It was

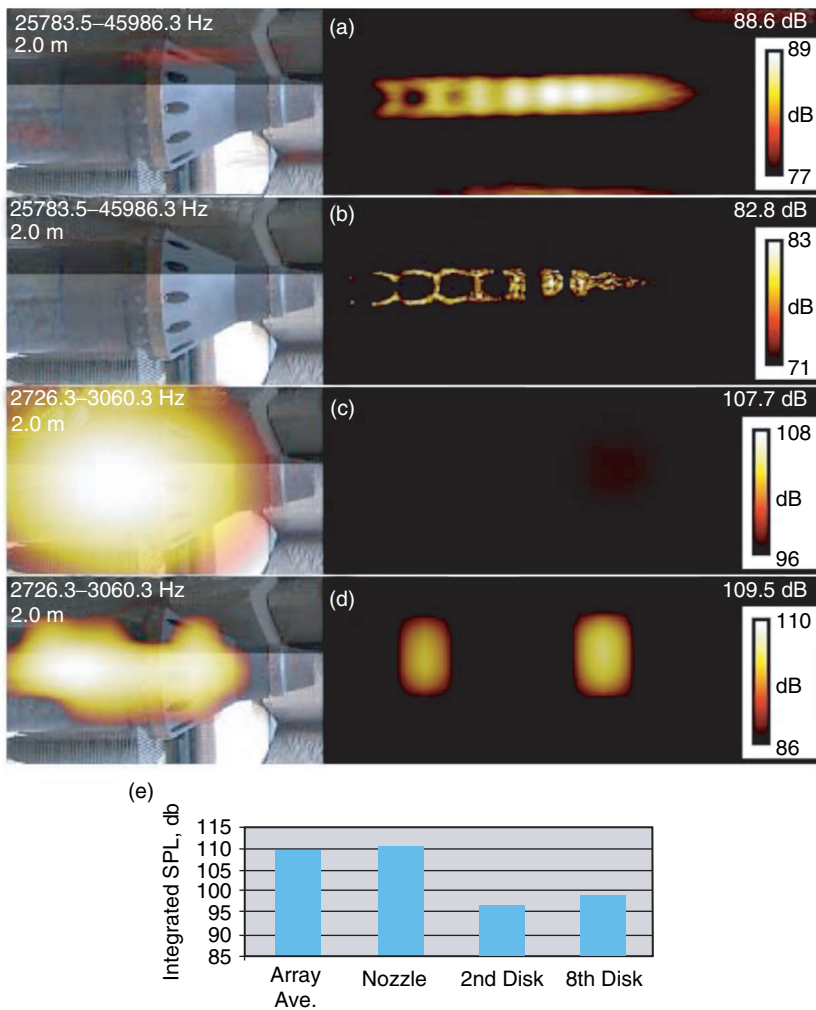


Figure 3: Beamform maps of a supersonic jet case using, (a) conventional beamforming at high frequency, (b) TIDY at high frequency, (c) conventional beamforming for screech tone, (d) TIDY for the screech tone, and (e) TIDY components breakdown for the screech tone (reprinted from Dougherty and Podboy [13]).

observed that using conventional beamforming the shock cell structure could be seen but was not very clear compared to the beamform map from TIDY. Figure 3(c) and 3(d) show the beamform maps of tonal noise using conventional beamforming and TIDY, respectively. Using conventional beamforming the source was located near the middle region of the pipe whereas TIDY revealed the noise origin to be the shock-cell screech sources. Upon separately calculating the contribution of each component, it was reported that the nozzle/pipe source was about 17 dB stronger than the source from the 2nd shock cell and about 11 dB stronger than the source from the 8th shock cell (see Figure 3(e)). These results show the power of using phased microphone array and beamforming in understanding and studying the complex mechanism of jet noise.

Performing experimental phased microphone array experiments on a jet facility is both expensive and has many limitations in terms of the array location and type of array to be used. Nelson et al. [20] were among the first to use the synthetic array technique, which combines the abilities of three different numerical tools to predict unsteady flow from a high speed jet, the resulting acoustics, and an analysis of noise sources. The Navier-Stokes equations are solved using the Compressible High Order Parallel Acoustics (CHOPA) solver to obtain an unsteady flow field in the

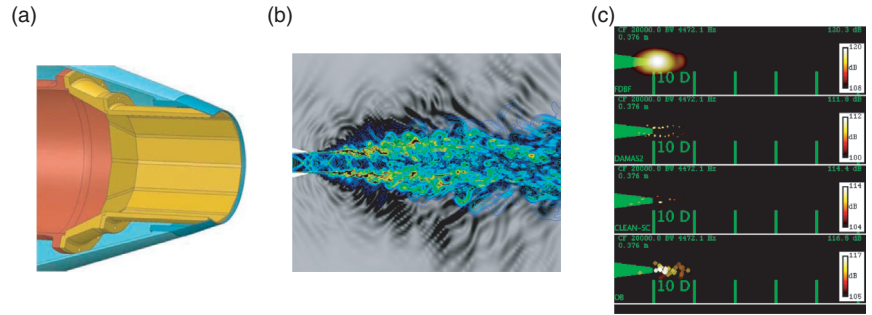


Figure 4: (a) Baseline military-style faceted nozzle geometry (design Mach number 1.5); (b) Instantaneous contours of density gradient magnitude (color) and pressure gradient magnitude (gray) in the $M = 1.36$ jet; and (c) Representative predicted noise sources using various beamforming methods at 4472.1 Hz. (reprinted from Nelson et al. [20], 2013 by the authors, used with permission).

vicinity of jet. Data from this solution is then fed into a Ffowcs Williams-Hawkings solver to predict the farfield acoustics. This prediction is used to record sound levels at virtual microphone locations, and the data is analyzed using a variety of beamforming algorithms. The baseline geometry for these cases is shown in Figure 4(a). A representative snapshot of an over-expanded jet ($M_j = 1.36$) flow field is shown in Figure 4(b). A sample result is shown in Figure 4(c). The plot shows predicted noise sources in a 1/3 octave band centered at 4472.1 Hz for different beamforming methods. The top sub-plot, which was created using frequency domain beamforming, shows the noise-producing region as a blurred mass in the vicinity of the nozzle, but no details are visible. The DAMAS2 algorithm appears to pick out structures in the jet shear layer. The CLEAN-SC algorithm, on the other hand, suggests the noise production is occurring further into the jet core. The Orthogonal Beamforming method, shown at the bottom of the plot, indicates a number of noise production peaks within the jet.

Panickar et al. [21] performed a detailed study on the feasibility and accuracy of applying beamforming to computational results. One of the major concerns when obtaining time-resolved HRLES simulation data is the amount of computational time required. The authors perform a study to determine the amount of time-resolved data required for acceptable beamforming results. The delay-and-sum beamforming was performed on a cold, overexpanded conic nozzle configuration using 128, 8 and 4 ensembles (see Figure 5). Reducing the number of ensembles from 128 to 8 significantly reduced the resolution of the beamform map but one was still able to distinguish the broadband shock associated noise and screech tone components. At 4 ensembles the beamform map degrades to an unacceptable condition. So based on this observation the author decide to select 6 ensembles of averaging as an acceptable number.

One of the main advantages of using this type of computational work is that it could provide guidance for optimal array design for similar experimental efforts. Figure 6 shows the beamform map of the jet from conic nozzle operated at pressure matched condition using different microphone arrays, such as the concentric microphone array, the log spiral microphone array and the large aperture log spiral array at different octave band center frequencies. The large aperture array provided better resolution at lower center frequencies than its small aperture counterparts whereas at higher center frequencies, the resolution is diminished due to large separation distance between the microphones in the large aperture array.

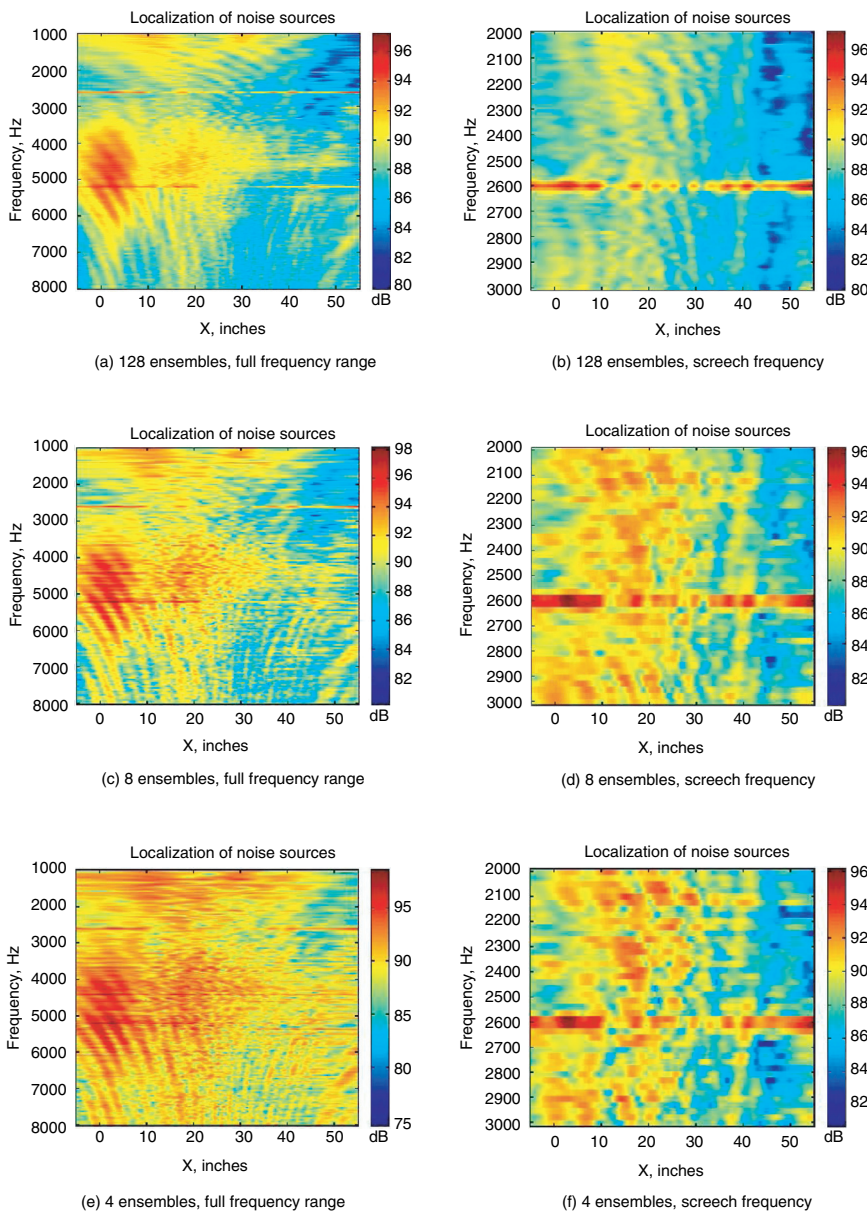


Figure 5: Beamforming results using the linear array of transducers on a cold conic nozzle with the centerbody operating at pressure matched conditions. (reprinted from Panickar et al. [21], 2013 by the authors, used with permission).

2.2.2. Wind turbine noise localization using a compact microphone array

In this section we describe the application of beamforming to wind turbines. The experimental study discussed here was conducted on a full-scale utility wind turbine located at the Invenergy wind farm at Grand Ridge, Illinois, USA. The wind turbine is a GE 1.5 MW wind turbine with a hub height of 85 m and a rotor diameter of 77 m. The turbine has a variable rotor speed of 10.1 to 20.4 rpm. The rated wind speed of this turbine is 12 m/s. The mean speed of the wind turbine during the field experiments was about 12 rpm, which corresponds to Mach number of 0.14 at the blade tip. The wind turbine is also equipped with state of the art wind speed and direction detection system known as ‘Catch the wind’. This system can detect wind speed and direction up to 300 m in front of the wind turbine. Based on the systems inputs the nacelle is controlled through yaw motors to change its direction to maximize the energy generated. The microphone array used for this study was the OptiNav Array 24 which has 24 microphones arranged

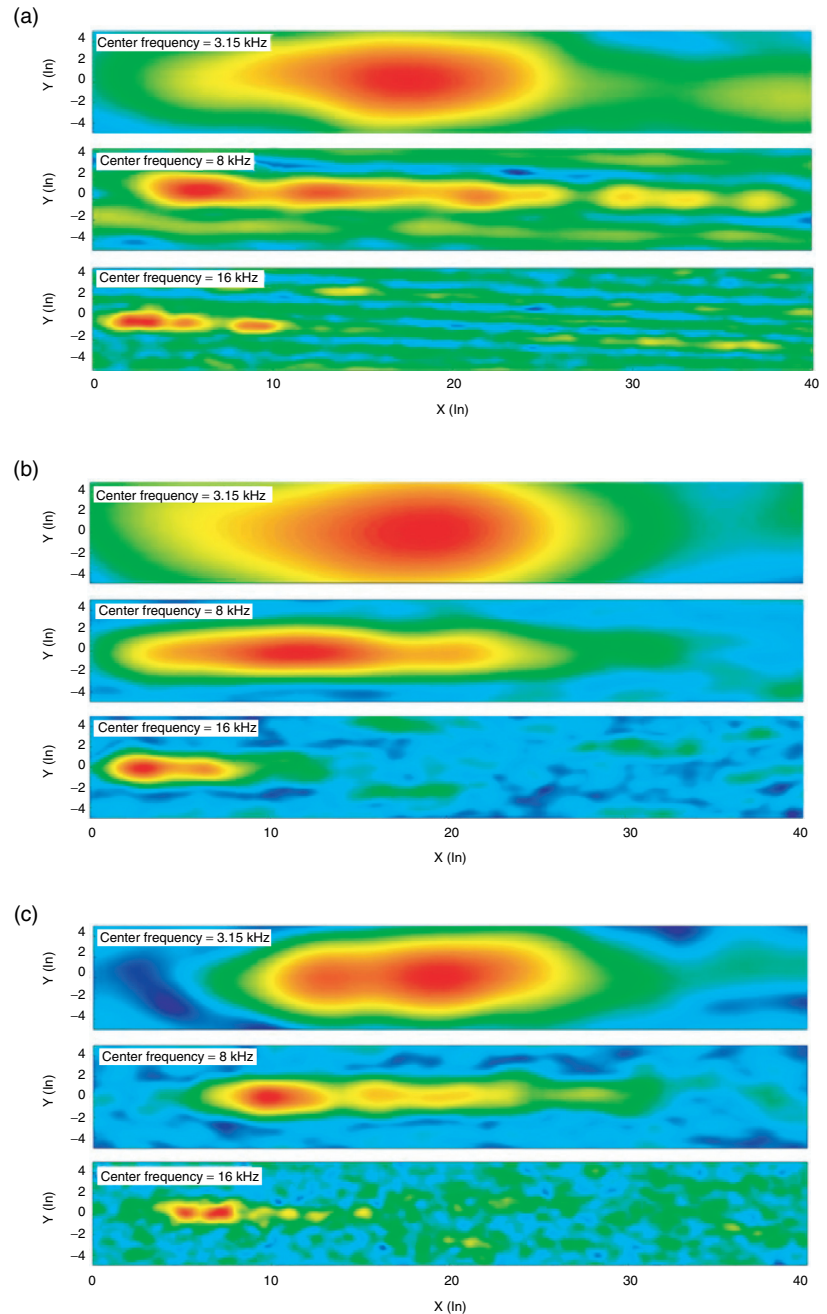


Figure 6: Beamforming maps for the jet from the conic nozzle with the centerbody operated at pressure matched condition using, (a) the concentric circular microphone array, (b) the log spiral microphone array and (c) the large aperture log spiral microphone array. (reprinted from Panickar et al. [21], 2013 by the authors, used with permission).

in a multi-arm spiral layout with the outermost sensors located at a distance of 0.72 m with a centrally located camera. The signal from the microphone array is acquired by an A/D converter which has 24 I/O audio interfaces. A MAGMA express box handles the task of interfacing the PCI 424 card to the computer. A USB cable connects the camera to a USB port on the computer.

The microphone array was qualified in the laboratory using different types of synthetic noise sources such as coherent and incoherent sources, stationary and non-stationary sources, and single and multiple sources. Detailed results of the qualification experiments are presented in Ramachandran and Raman [22].

CLEAN-SC generated accurate location estimates for narrowband frequency analysis when compared to DAMAS2 and FDBF. For broadband frequency analysis TIDY gave accurate location estimates when compared to DAS. The Rayleigh limit was also tested experimentally using synthetic sources: experimental results reaffirmed the theoretical findings. Detailed results of the Rayleigh criterion are discussed in Ramachandran et al. [23]. The first decision made before making the measurements was the location of the microphone array. The Rayleigh criterion provides an idea of the frequencies that could be resolved using the particular microphone array. The Rayleigh criterion is given by Eq. 45 [11];

$$W = rD / \lambda Z \quad (45)$$

where $W = 1.22$ is the Rayleigh limit that's the distance between the peak and the first zero of an ideal diffraction pattern below which multiple sources cannot be separated when using a particular type of imaging system. In the equation, r is the separation distance between the sources, D is the diameter of the array, λ is the wavelength of the source and z is the distance between the array and the source. The trailing edge noise of the wind turbine is believed to be in the range of 700 Hz – 2000 Hz [24]. The noise from the blade tip is also believed to be in the high frequency range. The aerodynamic noise is believed to be proportional to U^6 where U is the velocity [24]. Based on this knowledge of the aerodynamic noise, researchers selected two locations for the microphone array. The first location, L1, was at 50 m from the tower and the second location, L2, was at 85 m from the tower. Figure 7 shows the frequency curve obtained from the Rayleigh criterion to successfully separate the mechanical noise from the nacelle and the aerodynamic noise from the blades (particularly the blade tip and ends, say from $r = 35$ m).

Two locations were chosen for the placement of the microphone array. Location 1 (L1) was at 50 m from the tower and location 2 (L2) at 85 m from the tower. The schematic of the setup is shown in Figure 8(a). To get a clean beamform map where the various noise sources are clearly separable, advanced beamforming methods are necessary. Figure 8(b) shows the beamform map of the

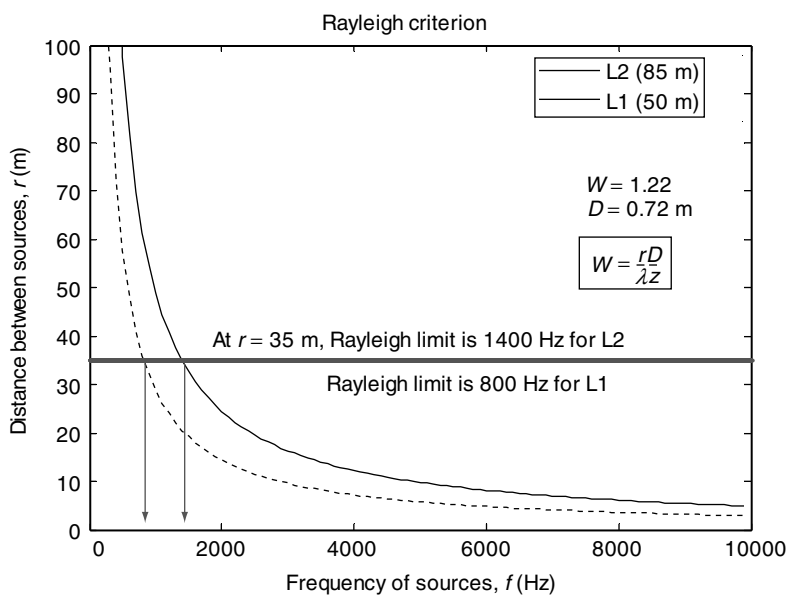


Figure 7: Frequency curve obtained from the Rayleigh limit to successfully separate noise from nacelle and blade tip. (reprinted from Ramachandran et al. [23], 2012 Multi-Science Publishing Co. Ltd., used with permission).

wind turbine over the frequency range of 108–10872 Hz obtained using the conventional DAS beamforming. From the beamform map it is clear that the noise sources, namely the mechanical noise from the nacelle and the aerodynamic noise from the blades are not clearly distinguished. When the beamforming is performed using an advanced method such as TIDY (see Figure 8(c)), the beamform map has clearly distinguishable sources. The mechanical noise from the nacelle and the aerodynamic noise from the blades are clearly distinguished. For this particular study the array was placed at location L2 and the plane of rotation of the wind turbine was parallel to the plane of the observer.

It could also be observed that the aerodynamic noise is asymmetric around the axis of rotation of the turbine. It can be more clearly observed in the aerodynamic noise shown in Figure 8(c). This asymmetry is attributed to the convective amplification effect i.e., as the noise source is a moving one, the noise source appears to be louder as it approaches the observer and appears to be less loud as it moves away from the observer. This behaviour was reported by Oerlemans et al. [25], where a large microphone array was used to characterize the wind turbine noise sources. In this particular case the blades of the turbine are rotating in counter-clockwise direction. From the models for trailing edge noise suggested by Brooks et al. [26], the convective amplification effect can be quantified using Eq. 46;

$$SPL_{CA} = 10 \log \left[\frac{1}{(1 - M \cos \theta)^4} \right] \quad (46)$$

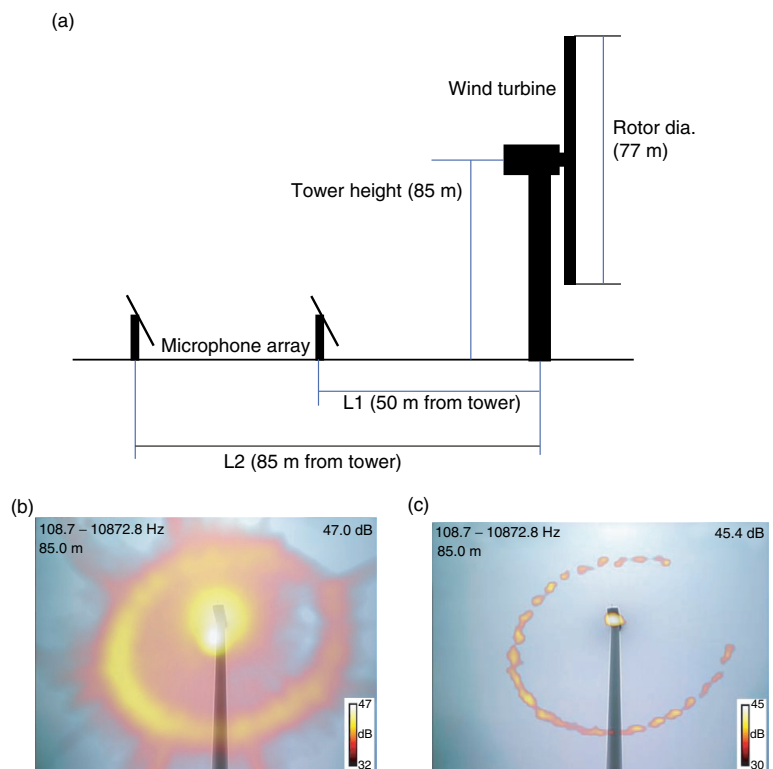


Figure 8: (a) Schematic of the experimental setup showing the two microphone array locations and the wind turbine. Beamform maps of a 1.5 MW wind turbine noise showing the effect of using; (b) an advanced beamforming method (TIDY) and (c) the conventional method (DAS). The frequency range for this map was 108 - 10872 Hz. (reprinted from Ramachandran et al. [23], 2012 Multi-Science Publishing Co. Ltd., used with permission).

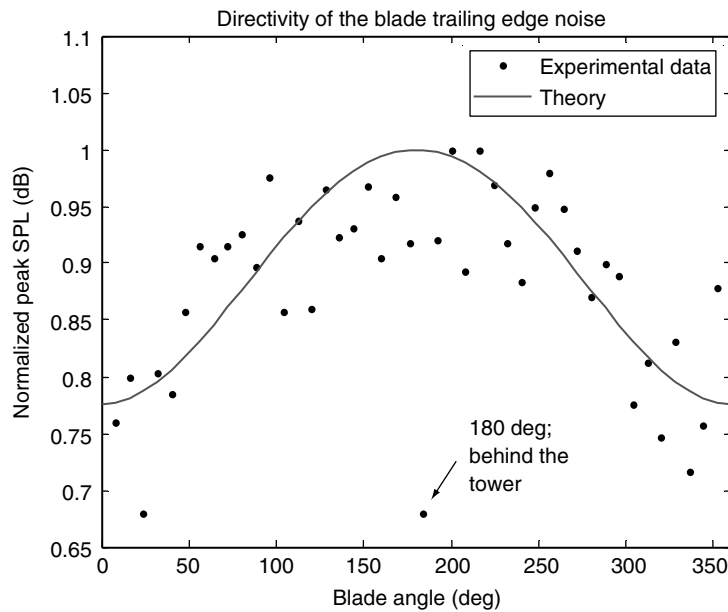


Figure 9: A comparison between the theoretical prediction and experimental result of the peak aerodynamic noise from the blade tip over one revolution. (reprinted from Ramachandran et al. [23], 2012 Multi-Science Publishing Co. Ltd., used with permission).

where θ is the radial angle of the blade and M is the Mach number of the blade. In this case, the Mach number of the blade was estimated to be 0.14 for the axial rotation of 14 rpm. The angle of the blade facing upward was assumed to be 0° and the blade rotates counter-clockwise. The SPL loss due to the convective amplification was calculated theoretically using the Eq. 46. The peak amplitude of the trailing edge noise was experimentally observed and normalized for comparison with the theoretical value. The comparison plot is shown in Figure 9. It is clear the experimental values compare reasonably well with the theoretical value. One interesting point in the experimental value is the sudden drop in amplitude at the rotation angle of 180° : is due to the fact that at 180° the blade was behind the tower of the turbine and the amplitude was masked resulting in this sudden drop in amplitude.

Figure 10 shows the beamform map obtained using DAS around the frequencies 1500, 3000 and 4500 Hz. The microphone array was at L2 and the Rayleigh frequency was calculated to be 1400 Hz. The beamform map becomes cleaner as the frequency increases. At 1500 Hz (see Figure 10(a)), the beamform map is inconclusive, whereas at 3000 Hz, the beamform map estimates can separate the aerodynamic noise from the mechanical noise. We can observe a considerable amount of side lobes prompted by researchers including auto powers in the calculation. At 4500 Hz the location estimates are cleaner. Figure 11 shows the beamform map obtained using TIDY for the same frequencies. We observe immediately that the beamform maps are much cleaner than the DAS beamform maps. Independently, a similar observation is made in TIDY beamform maps are cleaner with increase in frequency. A better beamform map is obtained using CLEAN-SC (see Figure 12). Both TIDY and CLEAN-SC suggest that there are four noise sources on the wind turbine: mechanical noise from the nacelle and aerodynamic noise from the three blades. The mechanical noise is justified whereas the aerodynamic noise is generally a distributed noise source along the length of the blades. The CLEAN-SC and TIDY locate them as a single peak close to the tip of the blades. Figure 13 presents the beamform maps obtained from DAMAS. We observe

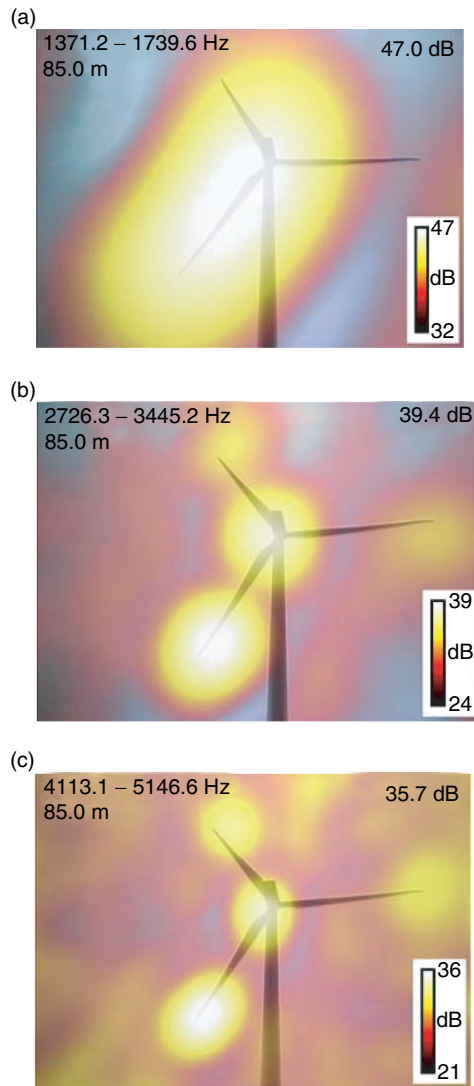


Figure 10: Beamform maps of the wind turbine noise using DAS around the frequency (a) 1500 Hz, (b) 3000 Hz, and (c) 4500 Hz. (reprinted from Ramachandran et al. [28], 2013 by the authors, used with permission).

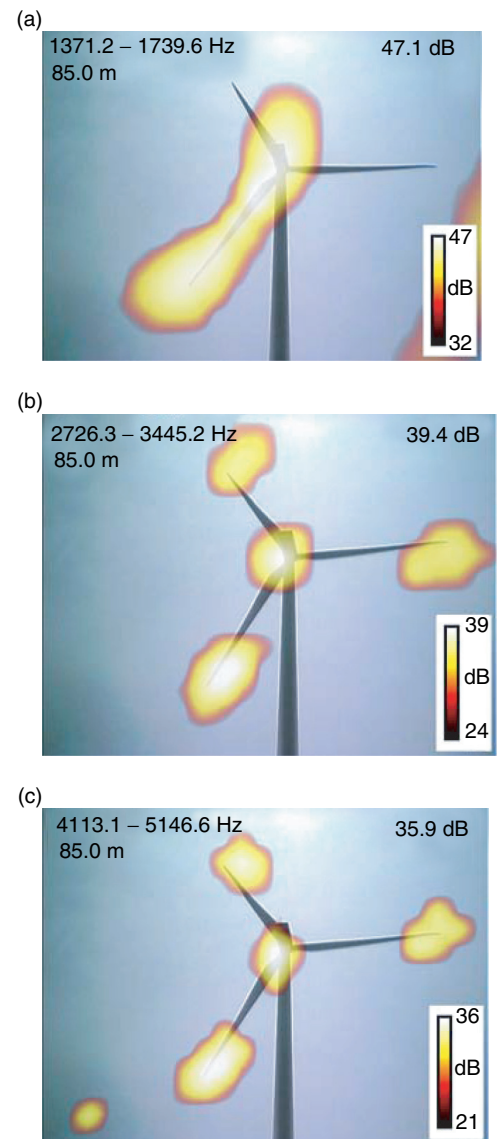


Figure 11: Beamform maps of the wind turbine noise using TIDY around the frequency (a) 1500 Hz, (b) 3000 Hz, and (c) 4500 Hz. (reprinted from Ramachandran et al. [28], 2013 by the authors, used with permission).

that DAMAS locates the mechanical noise from the nacelle in all cases and more importantly locates the aerodynamic noise on the wind turbine blades as multiple peaks distributed along the length of the blades. A new deconvolution algorithm, Deconvolution by Linear Programming, was developed recently by Dougherty et al. [27] and was applied to locate noise sources on a wind turbine by Ramachandran et al. [28].

2.2.3. Phased array experiments on detecting flow separation

In the experimental study performed by Perschke et al. [29], a backward-facing step induces a large-scale flow separation. One major difficulty with this approach is to discriminate between different sources of flow-induced sound. Turbulent flow over the edge of a backward-facing step produces trailing edge scattering noise that can dominate any other mechanism of sound production, especially at low Mach

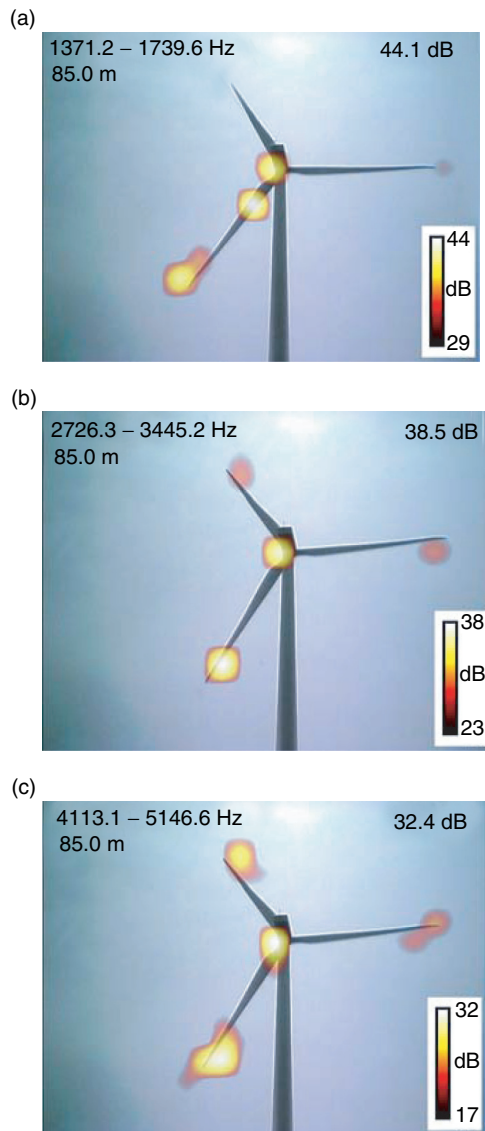


Figure 12: Beamform maps of the wind turbine noise using CLEAN-SC around the frequency (a) 1500 Hz, (b) 3000 Hz, and (c) 4500 Hz. (reprinted from Ramachandran et al. [28], 2013 by the authors, used with permission).

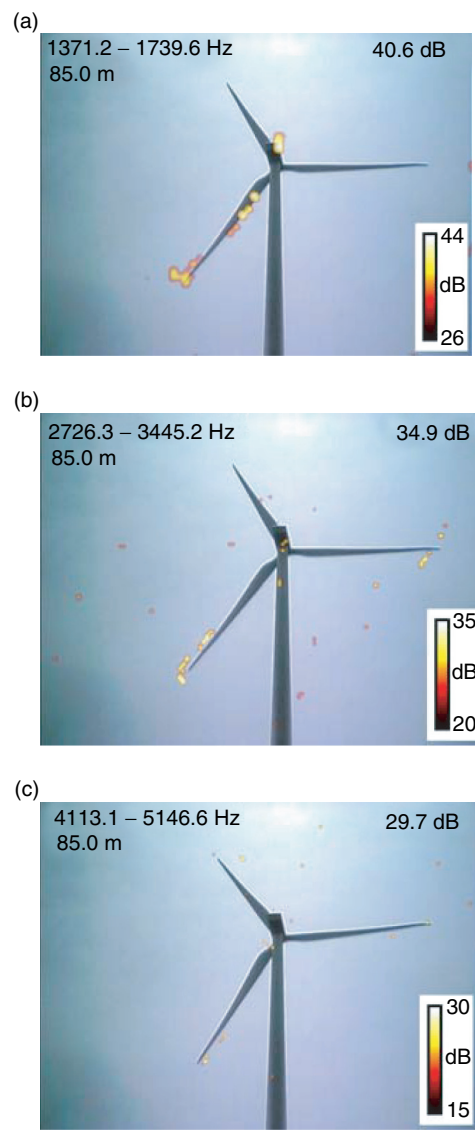


Figure 13: Beamform maps of the wind turbine noise using DAMAS around the frequency (a) 1500 Hz, (b) 3000 Hz, and (c) 4500 Hz. (reprinted from Ramachandran et al. [28], 2013 by the authors, used with permission).

numbers [30]. Dimensional analyses yield an eighth power law as a function of velocity for the acoustic intensity in the far-field produced by free-stream turbulence [31] and a sixth power law for turbulence in the vicinity of an acoustically compact rigid surface [32].

The experimental data was acquired at IIT's anechoic high-speed flow facility. Air is supplied at room temperature to a settling chamber. The jet exhausts into an anechoic chamber of dimensions $(2.2 \times 2 \times 4) \text{ m}^3$ through a rectangular jet opening of 6.35 cm width and 0.69 cm height. The backward-facing step is shown in Figure. 14(a). The step has a width of 15.24 cm and a total length of 38.1 cm. The upper part has a chord of 12.7 cm and the step height is adjustable from $h = 0 \text{ cm}$ to $h = 5.08 \text{ cm}$ in increments of 1.27 cm. The lower plate is terminated by a serrated trailing edge to reduce scattering of hydrodynamic pressure fluctuations. The test object allows for side walls to be mounted onto the plates, thus creating a channel of 5.08 cm height and 7.62 cm width between $y = \pm 3.81 \text{ cm}$. The backward-facing step is made

of aluminum and the material used for the removable side barriers is wood. During the experiments, the inlet was covered with foam. Two scenarios are considered: in the first case, no side walls are attached to the step, and in the second case, the side walls are attached to create a channel. The microphone array is placed at $(x, r) = (10, 50)$ cm at angles of $\theta = 15^\circ, 45^\circ, 90^\circ$ facing towards the jet centerline. In the case of the channel flow the observation angle is restricted to $\theta = 90^\circ$.

A comparison of the acoustic source maps generated by the algorithms TIDY, DAMAS2, and CLEAN-SC is presented in Figure 14(b). Beamforming is performed in a plane parallel to the array surface. The distance is set to $r = 50$ cm, and no fine-tuning of the distance parameter is performed. Moreover, no correction of mean-flow convective effects is attempted. The results for CLEAN-SC and DAMAS2 are obtained by summing the narrow-band array output over all frequencies of interest and TIDY used the covariance matrix of the entire wide-band frequency range. The array output power is color coded. The legend is shown in the lower right corner

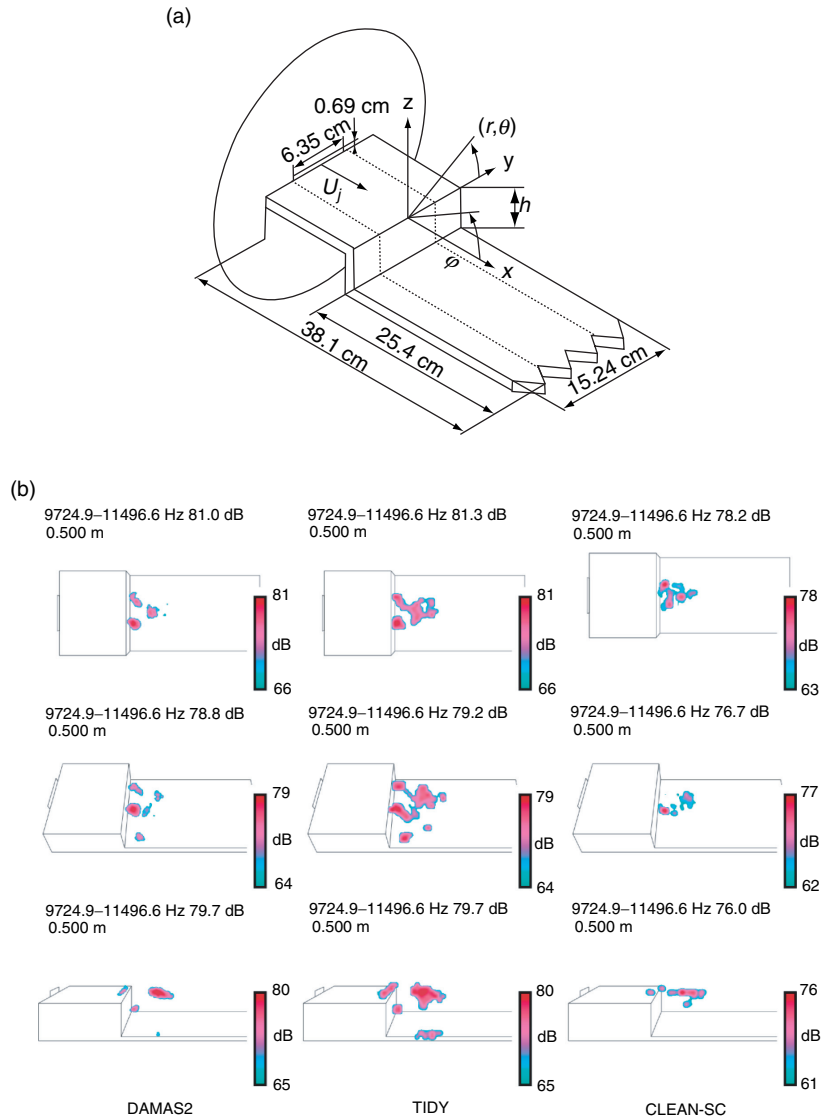


Figure 14: (a) Schematic drawing of the backward-facing step including the jet opening and the coordinate system, and (b) Comparison of the acoustic source maps obtained by TIDY, DAMAS2, and CLEAN-SC beamforming algorithms for $Ma = 0.6$ and $h = 5.08$ cm in the configuration without side barriers. (reprinted from Perschke et al. [29], 2012 by the authors, used with permission).

and the color scale is chosen such that the maximum output power corresponds to the highest value in the legend. Output powers that are not covered by the dynamic range of the legend are not displayed. The range of frequencies included in the beamforming process is shown in the upper left corner. The results demonstrate that the algorithms detect flow-edge interaction noise as well as free-stream turbulence noise. Two distinct sources are discernible near the trailing edge of the upper plate. A region of increased output power exists further downstream of the edge.

The peak output levels and locations of the maxima show good agreement between the algorithms although the results are not identical. The algorithms reveal the same main features of two distinct sources near the edge and a source region further downstream. DAMAS2 tends to yield clearer beamform maps and CLEAN-SC tends to suppress non-dominant output power. In the top view, the algorithms locate the maxima of the flow-edge interaction noise at $x = 1.66$ cm and the free-stream noise at $x = 4.72$ cm. Under $\theta = 45^\circ$, the maxima positions are $x = 1.72$ cm and $x = 6.35$ cm. Furthermore, DAMAS2 and TIDY detect a source region near the bottom plate at the streamwise location $x = 6.3$ cm and TIDY detects a second source near the lower plate at $x = 7.18$ cm. In the side view $\theta = 15^\circ$, flow-edge interaction maxima and the free-stream maxima are located at $x = 0.45$ cm and $x = 5.51$ cm. DAMAS2 and TIDY indicate a source near the bottom plate at $x = 6.86$ cm that cannot be observed in the results of CLEAN-SC.

The array output power of TIDY is summed over two regions of interest and normalized by the number of grid points in each area to determine the dependency of the different noise sources on Mach number and observation angle in the free step. Two regions are defined. The first encompasses the region downstream of the step ($2 \text{ cm} \leq x \leq 10 \text{ cm}$) and captures the free-stream noise. The second one encompasses the step ($-2 \text{ cm} \leq x \leq 2 \text{ cm}$). Both regions are shown in Figure 15(a). To allow for true separation of the different sources, the lower frequency limit is determined by the Rayleigh criterion for sufficient resolution ($f = 6800$ Hz) based on a distance of 4 cm. The upper frequency limit is the Nyquist frequency. The results are given in Figure 15(b). Subscripts denote multiples of the increment $h = 1.27$ cm in step height.

No reasonable values of the integrated output power or meaningful beamform maps in the regions of interest can be obtained for $M \leq 0.25$ in most cases. In fact, the source region near the nozzle generates most sound at these Mach numbers and frequencies. At all observation angles the array output levels follow a power law relation $I \propto U^n$ as a function of inflow velocity U . Linear least-squares fits are given as solid and dashed lines. For $\theta = 15^\circ$, the mean exponent for position 1 is $\langle n \rangle = 7.8(7.3...8.2)$ and for position 2 $\langle n \rangle = 6.5(5.8...7.3)$. The magnitude of the sound pressure under $\theta = 15^\circ$ is such that output power from position 1 is larger than at any other observation angle. Output power from position 1 displays the greatest difference to output power from position 2 of all observation angles. The output levels attain approximately the same magnitude at $M = 0.35$. As the observation angle increases to $\theta = 45^\circ$, output power from position 1 and 2 show the greatest difference in mean exponent of $\langle n \rangle = 7.8(7.1...8.4)$ and $\langle n \rangle = 5.8(5.5...6.0)$, respectively. Overall output powers from position 1 are comparable to the values obtained under $\theta = 15^\circ$, but for position 2 overall values are an average of $L_p = 7$ dB higher. Under $\theta = 90^\circ$, both sources show similar mean exponents of $\langle n \rangle = 5.4(5.1...5.8)$ and $\langle n \rangle = 5.1(4.8...5.4)$ for position 1 and 2 and overall output levels.

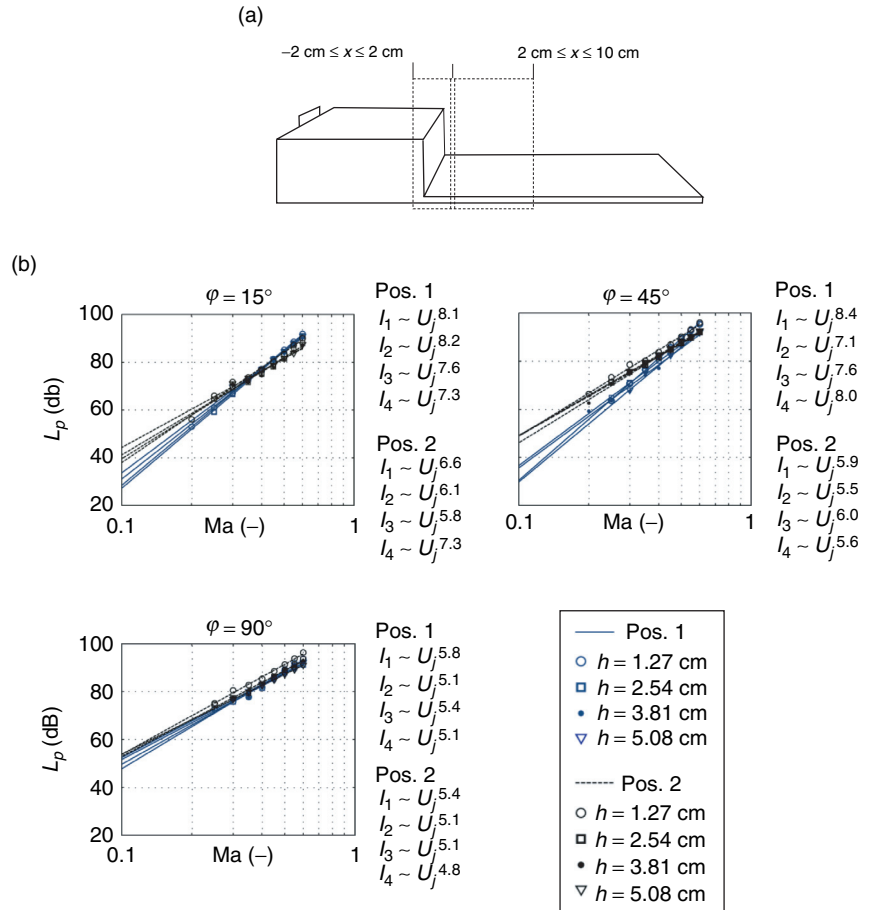


Figure 15: (a) Dashed boxes indicate the regions for the integration technique over the frequency range of $f = 6.8 \dots 22 \text{ kHz}$, and (b) Mach dependence of the array output power of two source regions. Position 1: $2 \text{ cm} \leq x \leq 10 \text{ cm}$, position 2: $-2 \text{ cm} \leq x \leq 2 \text{ cm}$. Subscripts denote multiples of the basic increment in step height $\Delta h = 1.27 \text{ cm}$. (reprinted from Perschke et al. [29], 2012 by the authors, used with permission).

2.2.4. Detecting air leakage in buildings using microphone array and beamforming

A room with significant air leakage was considered. An imbalance in the building's ventilation system caused a pressure difference (about 100 Pa) between the room and the external hallway. Gaps in the door of the room contributed most of the air leakage into the room. Figure 16 shows the door of the particular room in question. It also shows the possible locations for maximum air leakages (i.e., large gaps).

Tests were performed on the upper and lower halves of the door. Figure 17(a) shows the beamform map of the upper half of the door using the TIDY algorithm. In this we clearly observe the three sources of leak on the door. The pressure unsteadiness and sound associated with the airflow from these leaks could be detected by the array. The source for leak 1 is in the vertical gap between the two doors. Leak 2 occurs at the slot opening on the top of the door provided for the swivel mechanism and the source for leak 3 is at the gap between the door and the upper right hand side hinge. Figure 17(b) shows the beamform map of the lower half of the door using TIDY. The source for leak 4 occurs at the gap between the doors and the floor.

Additionally, results from another initial field test suggest that this acoustic technique coupled with an internal artificial acoustic source may also offer a

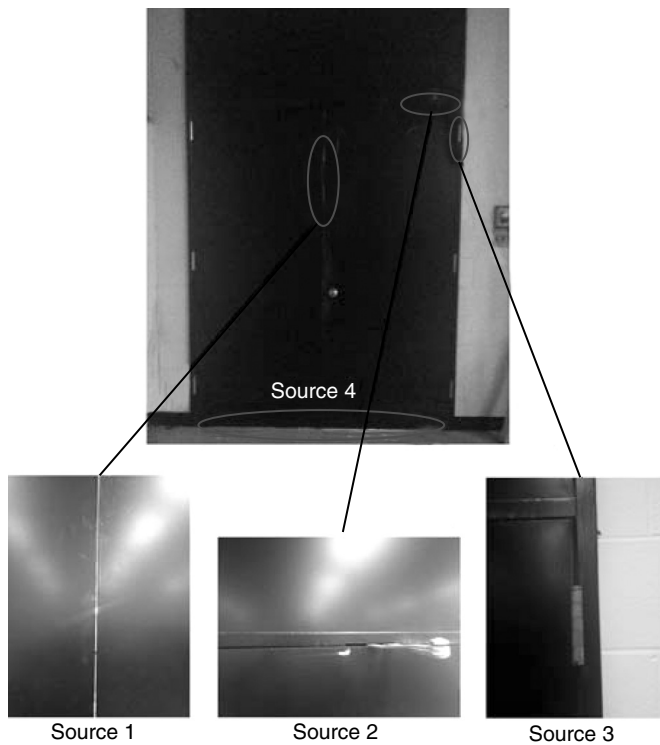


Figure 16: Schematic of the door with major air leakage spots indicated. A mechanically-driven pressure difference existed across the door under normal building operation. (Reprinted from Raman et al. [59])

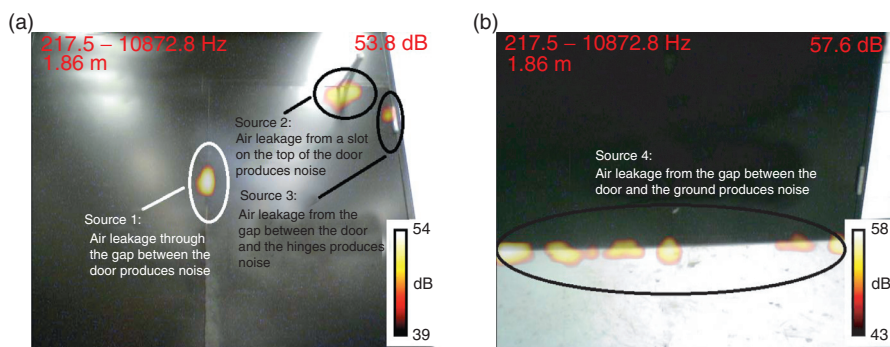


Figure 17: Beamform map of success at locating leakages from doors using the advanced wideband beamformer, TIDY of, (a) the top half of the door and (b) the bottom half of the door. The circled regions show the location and size of air leakage superimposed on the photograph of the door. (Reprinted from Raman et al. [59])

method for use without existing pressurization techniques, which if successful could be potentially very disruptive to existing methods. In this case, initial field tests were also performed on a building at IIT by placing an artificial acoustic source inside the room and locating the leakage spots using the acoustic phased array. Figure 18 shows the beamform map using the TIDY beamformer on the window of a room located in the first floor of the building. The artificial acoustic source was inside the room with the window slightly open (Figure 18(a)) and then wide open (Figure 18(b)). The yellow spots around the window (circled in red) indicate the location of significant leakage areas. There are also some locations close to the air conditioning unit that indicate air leakage areas around the unit.

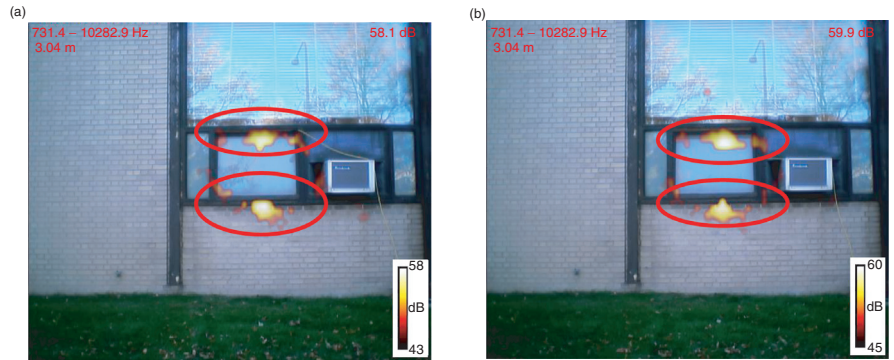


Figure 18: Beamform map of success at locating leakage spots in a window in the first floor of a building using the advanced wideband beamformer, TIDY with, (a) the window slightly open and (b) the window wide open.
(Reprinted from Raman et al. [59])

3. ACOUSTIC HOLOGRAPHY

3.1. INTRODUCTION

Near Field Acoustic Holography (NAH) came into use over 25 years ago as a means to identify the character of noise sources surrounding stationary vehicles. Measurements from a planar array of microphones placed close to a source can be projected to surface from which noise emanates. By separating the near field (reactive) pressure from the far field (acoustic) pressure, the true source of noise can be identified. The near field reactive pressures that dominate the measurement when microphones are close to a source are rejected by the processing leaving only the portion that would propagate to the far field.

NAH is quite different from the conventional acoustic holography (as well as optical holography) and has the following qualities, (a) One can obtain the result fields in three dimensional domain from the measurements made at a two dimensional plane (as any other holography method). (b) In addition to the field corresponding to the measured quantity (say acoustic pressure), fields of derived quantities such as particle velocity, directivity pattern can be calculated easily in three dimensions. (c) It is possible to obtain temporal evolution of fields. The conventional holography used a single wavelength source to construct and reconstruct the hologram that has an inherent disadvantage that the resolution is limited by the wavelength. However, in NAH, the resolution is limited only by the dynamic range of the measurement system and distance between the source and hologram surfaces. See Maynard and Williams [33] for more details regarding the advantages of this technique.

Most of the recent research on NAH falls under one of the following three categories:

- Fast-Fourier Transform (FFT) based NAH for conformal geometry sources – namely planar, cylindrical and spherical ([33], [34])
- Boundary Element Method (BEM) based NAH for complex shaped sources [35]
- NAH based on modern techniques such as Equivalent Source Method (ESM), Spectral Decomposition Method (SDM), or Helmholtz least-squares for complex shaped sources (e-g) [36]

Spatial FFT based methods are suitable when the source surface is conformal to the hologram surface. Despite its simplicity this method is not desirable in most situations as the number of measurement points in the hologram surface affects the resolution when we use the two dimensional FFT. The boundary element method

is the most famous tool due to its minimal computing requirements (as only the mesh is needed only on the boundary) and its ability to deal with smooth and sharp complex surfaces. Modern methods are evolving rapidly to develop the NAH technique as a tool for non-destructive testing of sound and vibration sources. Recently, the research interest has shifted towards the development and implementation of regularization and solving methods (for solving the equations arrived using BEM or ESM) (e-g) [36]. These techniques empower the NAH to deal with the problematic frequency zones also. For example, one can use LU decomposition (where L stands for lower triangular matrix and U stands for upper triangular matrix) to determine the condition number of the matrix obtained using BEM. If the matrix is ill-conditioned, then a method such as singular value decomposition could solve (instead of Gauss elimination or other classic solvers).

3.2. IMPLEMENTATION OF NAH IN WIND TUNNEL

An implementation in a wind tunnel environment using the linear array shown in Figure 19 differs from classical planar holography Long and Martens [37]. In this case the effects of convection cannot be ignored and the processing must account for the pressure fluctuations associated with the turbulent boundary layer riding over the surface of the flush transducers. Convection is addressed by appropriate modification to the dispersion relation between frequency and wave number. The subsonic boundary layer is rejected because it consists of hydrodynamic non-propagating fluctuations. The measurement consisting of the cross-spectral matrix from every transducer pair is mathematically propagated outward to the far field and inward toward the source region. The outward propagation produces far field results as though the measurement is actually conducted in the far field. The inward propagation provides intimate details of the source region Long and Martens [37].

The procedure adopted here is often called Spatial Transformation of Sound Fields (STSF) that relies on principal component analysis (the Singular Value Decomposition) to separate the measurement into orthogonal subspaces. The first step is to compute the full cross spectral matrix (CSM) as the outer product between all transducer pairs. The next step is to divide the measured CSM into its fundamental fluctuation modes via Principal Component Analysis (PCA). Other names for this tool are The Proper Orthogonal Decomposition or the Karhunen-

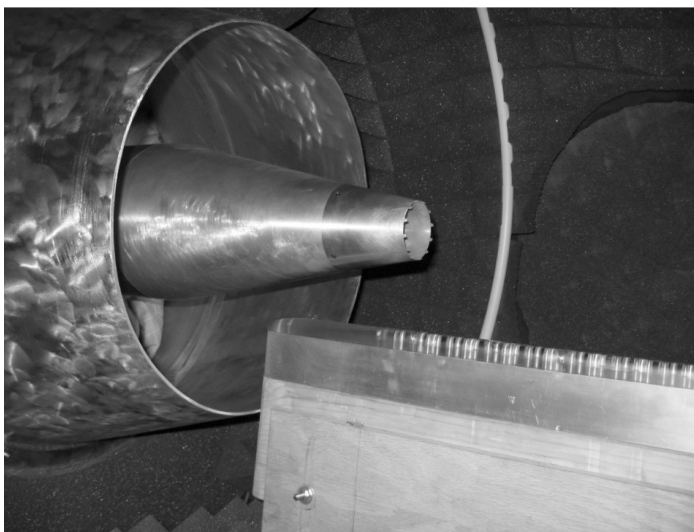


Figure 19: Picture of the linear microphone array setup for Nearfield Acoustic holography (NAH). (reprinted from Long [37], 2009 by the authors, used with permission).

Loeve Expansion. This leads to a matrix eigenvalue equation,

$$C_{ij}K_j^n = |\lambda_n|^2 K_i^n \quad (47)$$

The eigenvalue λ^2 represents the energy content and the eigenvector K_i represents the characteristic signal form at the i^{th} transducer location. The signal portion of the n^{th} partial field spectrum can be identified as,

$$S^n(x, \omega) = \lambda_n K^n(x; \omega) \quad (48)$$

Then the signal $S(x, \omega)$ is “propagated” to a new radial distance using a propagation operator: accomplished in the wave number domain obtained from the spatial Fourier transformation of S ,

$$S(k_x, \omega) = \int S(x, \omega) e^{-ik_x x} dx \quad (49)$$

In this equation k_x represents the wave number along the measurement axis. It should not be confused with the acoustic wave number $k_a = \omega/a$. The relationship among k_a , k_x , and k_y is described by the Pythagorean triangle,

$$k_y = [(\omega/a)^2 - k_x^2]^{1/2} \quad (50)$$

In fact, it is precisely the difference between k_x and k_a that allow the measurement radius, y_m , to be propagated to the desired radius, y_p , via the propagation operator,

$$S(k_x; y_p) = (y_m / y_p)^{1/2} S(k_x; y_m) e^{ik_y(y_p - y_m)} \quad (51)$$

The first term provides the radial divergence, and the second term provides the wave pattern due to the axial variations. The true functionality is based on a Hankel Function derived from the Bessel Function of the first and second kind, but this approximate equation is valid for all regions of interest outside the plume, which ensures that the total acoustic energy remains constant on all cylinders surrounding the jet axis.

An example of a typical source distribution at supersonic conditions is shown in Figure 20(a). The vertical source features are directly associated with the shock cells in the jet plume and are easily identified using shadowgraph images Long and Martens [37]. A spark source projects light that passes through the exhaust plume and a ground glass imaging plane on the opposite side of the plume from the spark sends diffracted light toward the camera, which freezes the structure of the flow identifying regions with large density gradients – such as shock and expansion waves. The location of the normal shocks in Figure 20(b) correspond with the vertical sources in Figure 20(a).

4. SIMULTANEOUS FLOW/ACOUSTIC MEASUREMENTS

4.1. PHASE AVERAGED MEASUREMENT TECHNIQUE

Phase-locked measurements for capturing resonant oscillations such as screech, and phase-averaged measurements have been commonly used in the last couple of decades. Nevertheless, this simple technique is capable of providing useful information with limited experimental resources. The reason for including this well known technique in an article on advanced techniques is the simplicity and cost-effective nature of these measurements. For instance, the first example illustrates how just two microphones can

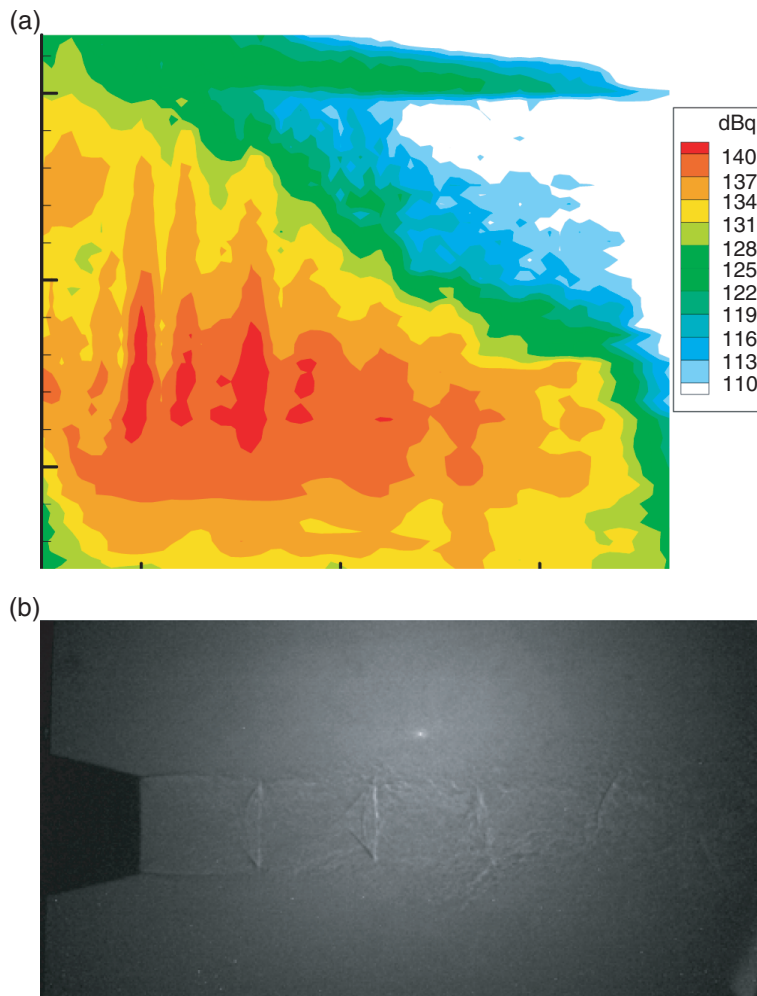


Figure 20: *Acoustic holography. (a) Microphone array (b) Acoustic map compared with a spark shadowgraph image (reprinted from Long [37], 2009 by the authors, used with permission).*

perform phase averaged measurements to visualize twin-jet coupling in symmetric and antisymmetric modes.

The objective of this exercise was to obtain the acoustic pressure pattern over twin-nozzles in various coupling scenarios (see Panickar et al. [38] for details). To obtain the phase averaged readings, researchers placed the reference microphone in between the two nozzles and the measurement microphone was traversed in the spanwise direction at a certain height (see Figure 21). At each measurement location, time series data for both the microphones were acquired. The reference signal was digitally filtered around the screech frequency in order to enhance the tonal (sinusoidal) content. The signal from the measurement microphone at each location was triggered at selected phase angles of the screech cycle from the reference signal. Finally, the sound pressures at the triggered phase angles were ensemble averaged, to obtain the average sound pressure corresponding to that particular phase angle. Figure 22 shows the phase averaged picture along a line, for an inter-nozzle spacing of $s/h = 7.4$ at a fully expanded jet Mach number of 1.33. In this figure, the curves represent the pressure distribution in the spanwise direction, for a particular position (phase) in the screech cycle. Thus, 24 curves, separated at 15° intervals represent the activity over a cycle (360°) as shown in the figure. For clarity, subsequent curves are translated vertically by 70 Pa. Figure 22 clearly shows that the jets are coupled in a spanwise symmetric mode at Mach number 1.33

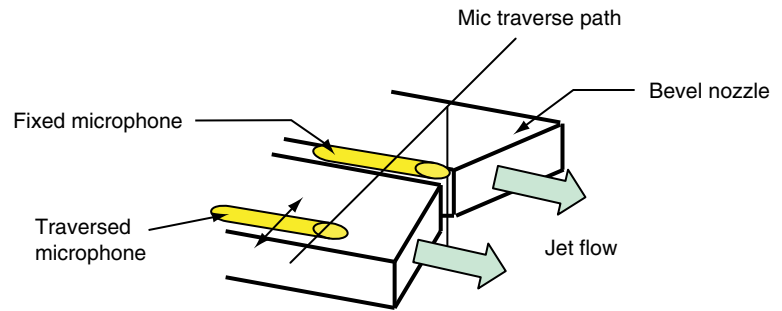


Figure 21: Schematic of Twin beveled nozzle in a V shape configuration. (reprinted from Panickar et al. [38], 2003 Elsevier Ltd., used with permission).

(Figure 22(a)) and at spanwise antisymmetric mode at a higher Mach number of 1.46 (Figure 22(b)). These measurements were independently corroborated with phase measurements using two spanwise microphones. Nevertheless, the actual pressure patterns over the nozzles provides in-depth visualization of the nature of twin-jet coupling that would not be available in simple two-point phase measurements.

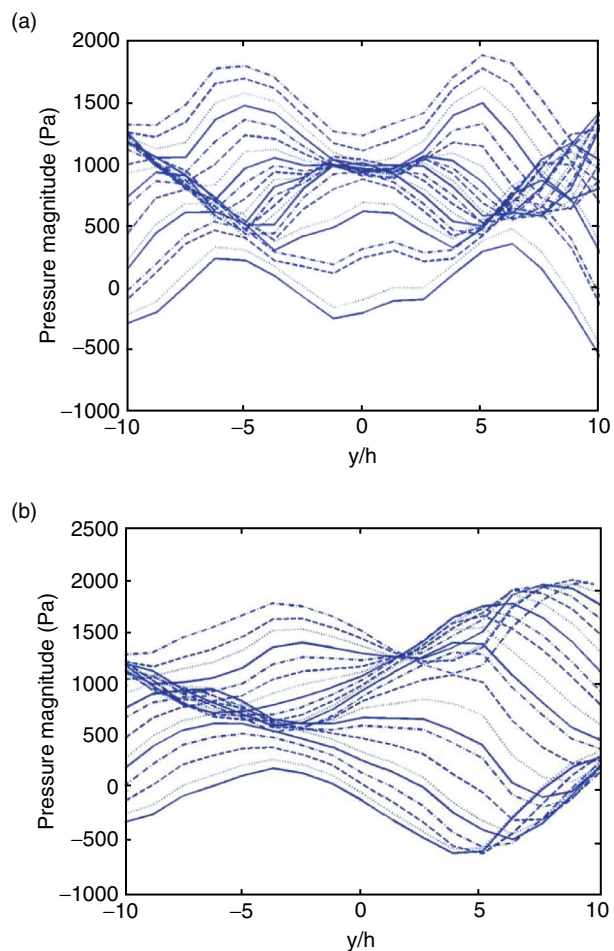


Figure 22: Phase averaged acoustic pressure measurements in jets exiting from twin beveled rectangular nozzles. (a) Acoustic pressure pattern in symmetric coupling at Mach number 1.33 (note the symmetric lobes). (b) Anti-symmetric coupling of the twin jets at Mach number 1.46. (reprinted from Panickar et al. [38], 2003 Elsevier Ltd., used with permission).

Sarpotdar et al. [39] used phase averaging to unravel the near-field pressure directivity in Hartmann whistles. Pressure transducer was traversed in the near-field to obtain phase-averaged images that indicated regions of high acoustic intensity and hence directivity. Such results could be used to correlate them with acoustic directivities measured in the far field. Figure 23 shows an example of such source location in a powered resonance tube obtained using phase-averaged measurements [39].

The pioneering works of Panda and coworkers ([40-43]) on simultaneous flow/acoustic measurements have been chosen to illustrate the strength of this technique. The subject of jet noise has been aspiring for tools that (i) identify noise sources and (ii) explain the mechanisms operating in these sources. While several techniques including those presented in this article could achieve goal (i), there are very few successful attempts that explain noise source behavior. Samimy

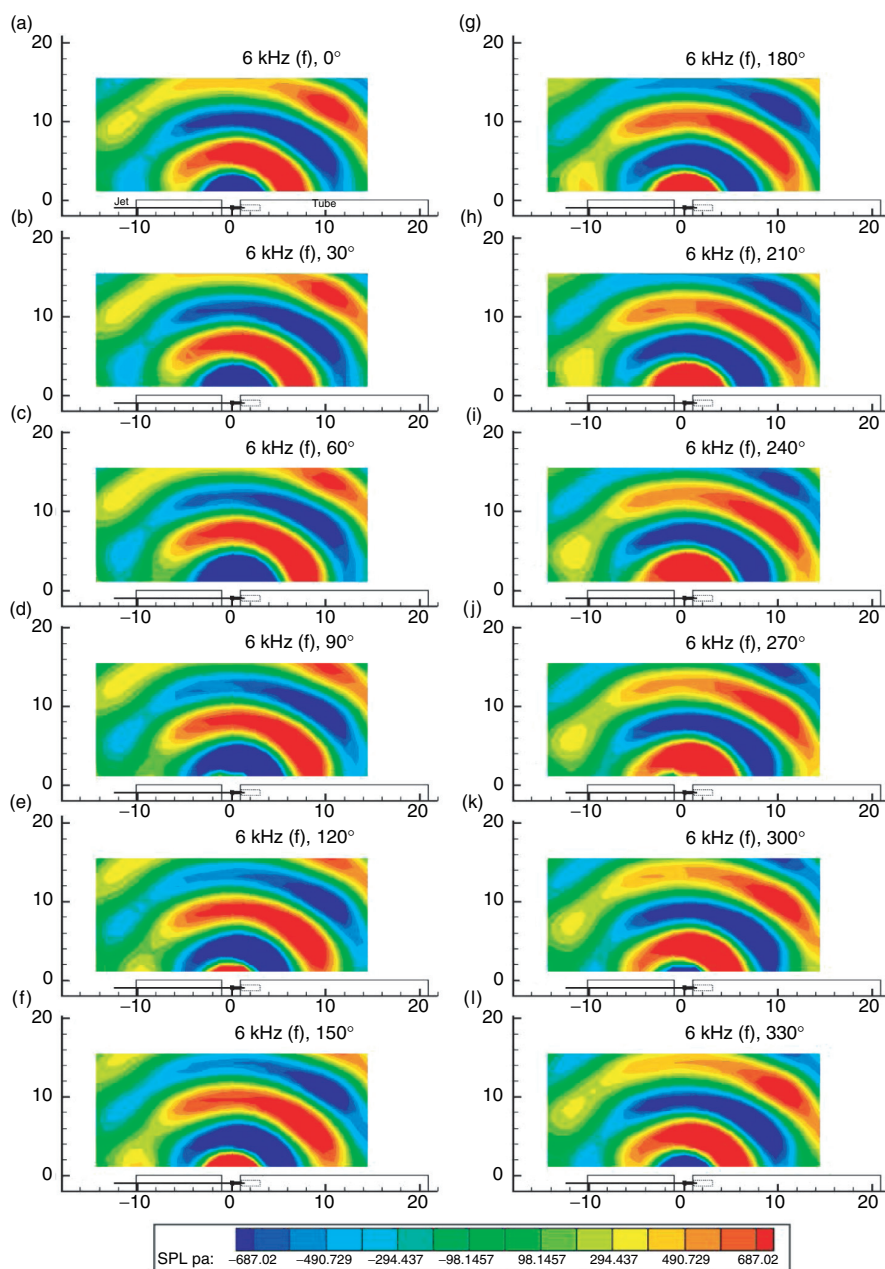
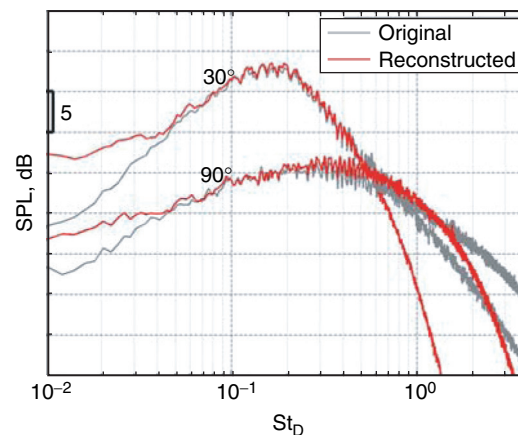
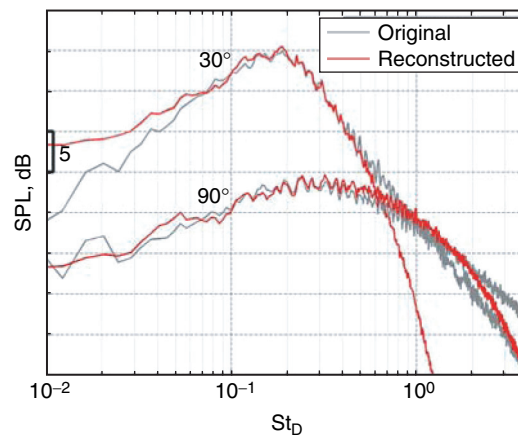


Figure 23: Acoustic Phase averaged measurements in the near field of a powered resonance tube. (reprinted from Sarpotdar et al. [39], 2005 Springer-Verlag, used with permission).

and co workers ([44-49]) performed significant work on large-scale structures and their correlation to the peak noise at shallow angle using simultaneous flow/acoustic measurements and phase averaging using jet excitation. Their work started in 2005 [44] by looking at time traces of far-field acoustic signal (rather than conventional power spectrum) and correlating high amplitude randomly occurring events at shallow angles to the jet axis to large-scale structures in the jet. They showed that these events correlate with the interaction and disintegration of large-scale structures around the end of potential core. Their recent work [47] using a large data base from NASA Glenn Research Center models these events using a Mexican hat function and shows that one can reconstruct the far-field spectra at shallow angles using only these events, that constitute less than 15% of the entire acoustic signal (see Figure 24). In addition, their results indicate the average time between these events correlate well with the Helmholtz number of the peak of the spectrum (see Figure 25) and that there is a strong correlation between the average time between the events and duration of the events (see Figure 26). The last finding indicates that the noise events produced by large-scale structures are more organized than the structures generating them. Their recent jet excitation and phase averaging have started revealing the nature flow structures and noise sources [48, 49]. For example, they vividly show the effects of jet parameters and the nature of jet structures on the onset and evolution of Mach wave radiation [48] (see Figure 27).



(a) $D = 2.54$ cm, $TTR = 1.00$, $M_a = 0.9$



(b) $D = 5.08$ cm, $TTR = 2.84$, $M_a = 0.9$

Figure 24: Example spectra for signal reconstruction. (reprinted from Kearney-Fisher et al. [47], 2013 by the authors, used with permission).

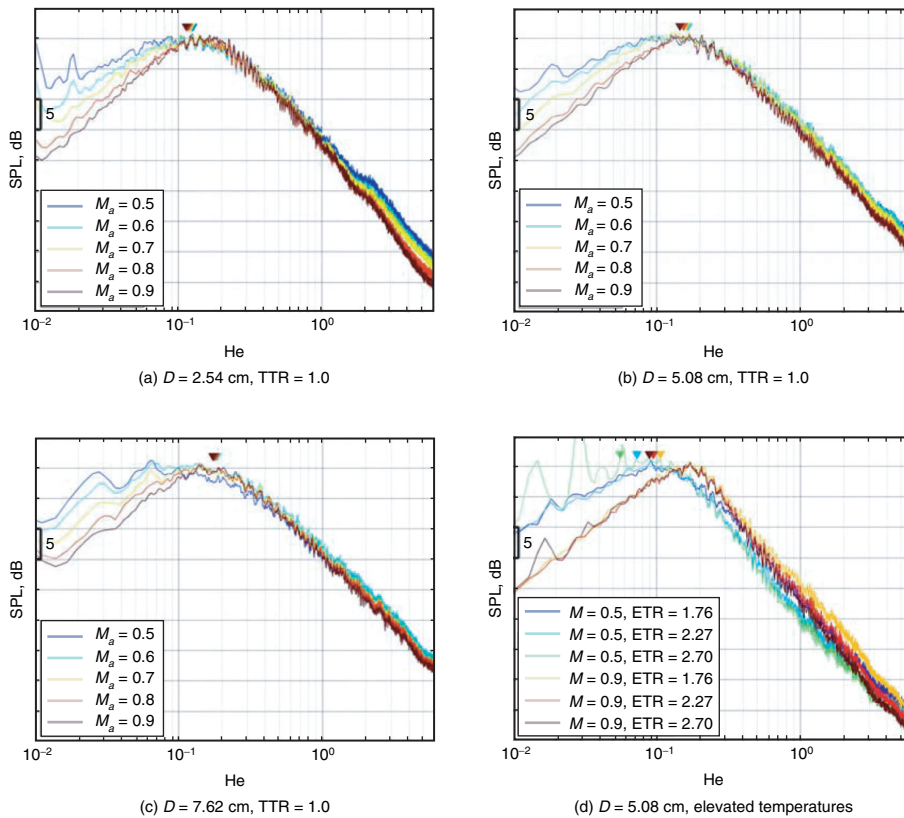


Figure 25: Spectra at $\Phi = 30$ deg showing the predictive capability of mean intermittence. (reprinted from Kearney-Fisher et al. [47], 2013 by the authors, used with permission).

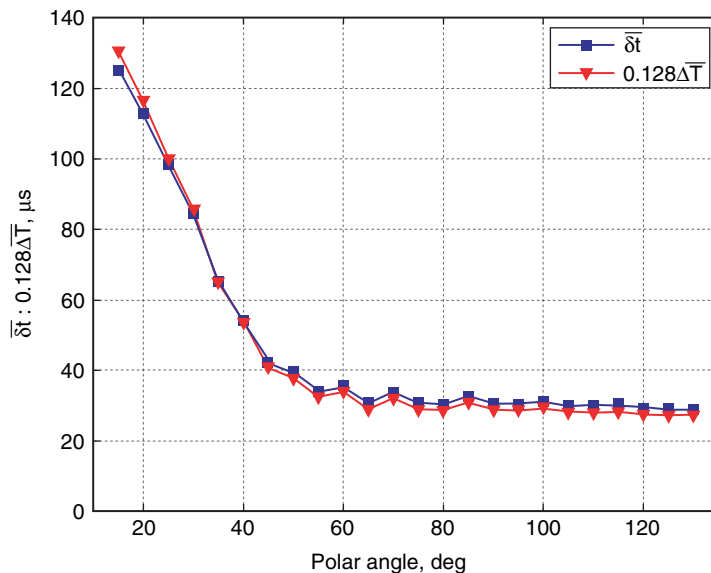


Figure 26: Directivity pattern of mean width and intermittence for case 5 ($D = 2.54$ cm, $M_a = 0.9$, and $TTR = 1.0$). (reprinted from Kearney-Fisher et al. [47], 2013 by the authors, used with permission).

4.2. TWO POINT MEASUREMENT TECHNIQUE

Panda et al. [40] simultaneously measured fluctuating velocities and densities along with acoustic pressures. The flow variables were measured based on a molecular Rayleigh scattering technique using a Fabry-Perot interferometer. From the measurements of fluctuating velocities and densities, they calculated correlations

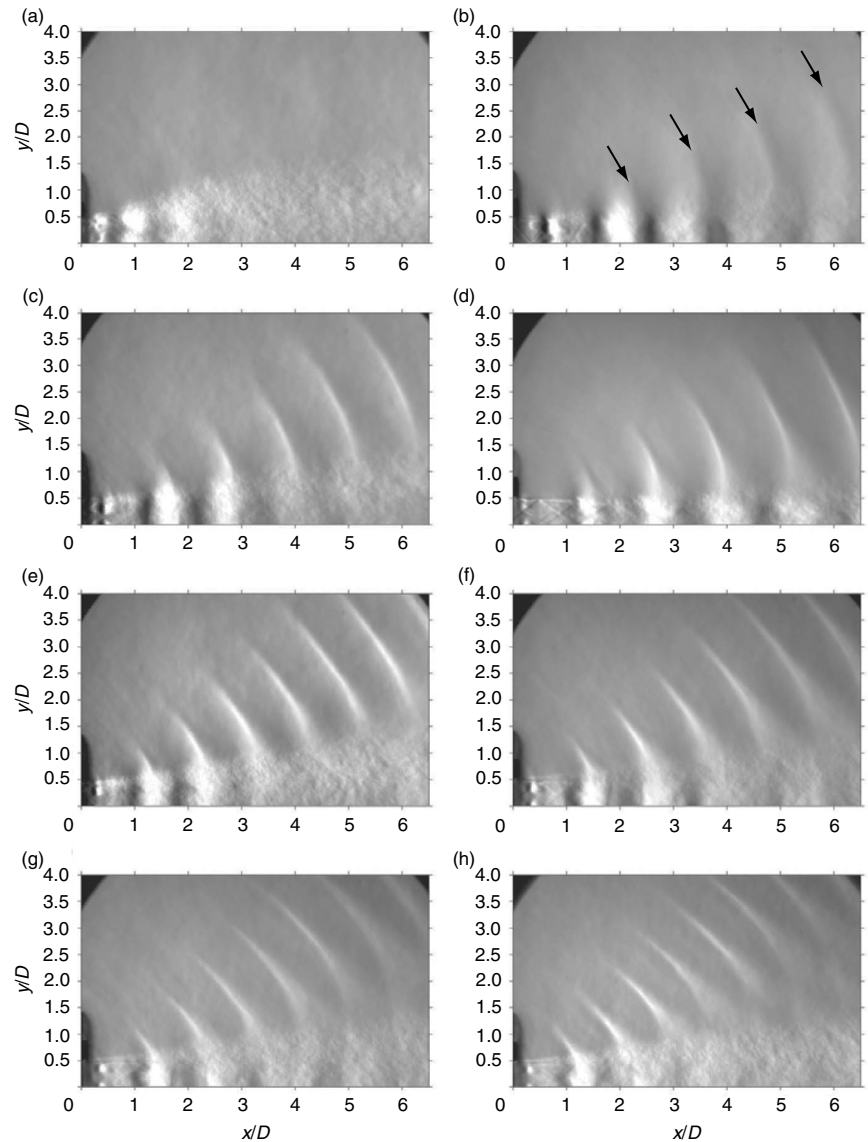


Figure 27: Schlieren images of jets at various operating conditions forced with $m = 0$ at $St_{DF} = 0.6$: (a) $M_j = 0.9$, $T_j/T_\infty = 2.5$; (b) $M_j = 1.3$, $T_j/T_\infty = 1.25$; (c) $M_j = 1.3$, $T_j/T_\infty = 1.75$; (d) $M_j = 1.65$, $T_j/T_\infty = 1.1$; (e) $M_j = 1.3$, $T_j/T_\infty = 2.5$; (f) $M_j = 1.65$, $T_j/T_\infty = 1.6$; (g) $M_j = 1.65$, $T_j/T_\infty = 2.0$ and (h) $M_j = 1.65$, $T_j/T_\infty = 2.5$. (reprinted from Kearney-Fisher et al. [48], 2011 Cambridge University Press, used with permission).

between the flow and acoustic pressure. The peak correlation values were plotted against axial distance, which revealed that correlation values are small inside the potential core and increase downstream of the potential core. This was attributed to the merging of the shear layer and fragmentation of large scale structures and concluded as a possible sound generation source. Similar correlations were performed by Panda to illuminate the effect of velocity in heated jets. Correlations plotted against axial distance along peripheral and central locations revealed that under supersonic conditions, peripheral layers become efficient acoustic radiators, and the correlation frequency range widens. Thus, simultaneous measurement of flow and acoustic quantities are necessary to unravel the coupling between hydrodynamic mechanisms and the acoustic consequences. Figure 28 shows the schematic of the setup for the two point measurement technique.

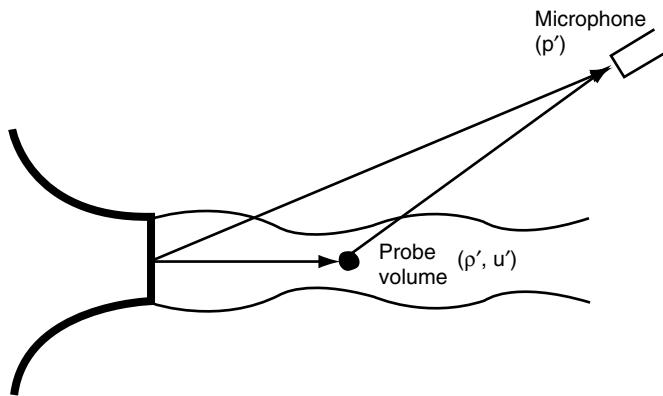


Figure 28: Schematic of the two-point measurement setup. (reprinted from Panda et al. [40], 2005 Cambridge University Press, used with permission).

Figure 29 presents normalized $\langle \rho; p' \rangle$, $\langle \rho u u; p' \rangle$ and $\langle \rho v v; p' \rangle$ cross-correlations from 150° and 90° microphone polar angles. The $\rho u u$ product was created by multiplying density $\rho(t)$ and velocity $u(t)$ time-traces. The cross-correlation values were calculated via Fourier transform, that is the cross-spectrum $P_{\rho u u; p'}$ and $P_{\rho; p'}$ were calculated first, and then inverse transforms were taken to return to the time domain. Figure 29 prompts multiple interesting observations.

1. Air density fluctuations show as good a correlation as ρ_{uu} ; even the time variations of the correlation data are similar. The same was found to be the case for the correlation with the axial velocity fluctuations $\langle u; p' \rangle$. Therefore, it can be said that the noise sources can be expressed in many different variables.
2. There are other variables which show far poorer correlation. Unlike ρ_{uu} , ρ_{vv} shows significantly lower correlation with the far field noise. That the $\langle \rho_{vv}; p' \rangle$ correlation with a 90° microphone is immeasurably small is of particular interest. The causality relation dictates that $\langle \rho_{vv}; p' \rangle$ correlation as the source for the 90° noise. Therefore researchers expected that $\langle \rho_{vv}; p' \rangle$ correlation from a 90° microphone would be significant, but it was not. Similarly, causality relation shows that ρ_{vv} fluctuations has little to do with the 150° noise radiation, yet microphone signal from this angle show significant $\rho_{vv}; p'$ correlation above the noise floor.
3. Sound pressure fluctuations at 90° to the jet axis correlate poorly with any flow variables. An exception was found in $\langle \rho; p' \rangle$ correlation in highly heated jets.
4. The time duration $\Delta\tau$ over which correlation changes from zero to negative to positive and back to zero is significantly long. For the particular $Ma = 0.95$ jet, $\Delta\tau$ is estimated as 1.2 msec. This provides a measure of coherence time of the dynamic process responsible for sound radiation. Invoking Taylor's hypothesis, the corresponding coherence length scale is $l_{\text{coher}} = \Delta\tau U_c$, where U_c is the convective speed. Assuming $U_c = 0.7U_j$ the coherence length $l_{\text{coher}} \approx 10D$. In other words, the longest source contributing towards correlation is, on an average, 10 jet diameters long. Therefore, the noise source responsible for sound radiation, at the shallow 150° angle, is indeed "non-compact."

Strouhal frequencies for two different Mach number jets are shown in Figure 30. For this figure a large number of correlation data were measured by moving the laser probe from point to point in the flow, while keeping the microphone location fixed. Later, coherence values at a desired Strouhal frequency were isolated for all measurement stations and plotted using indicated color scale. Note

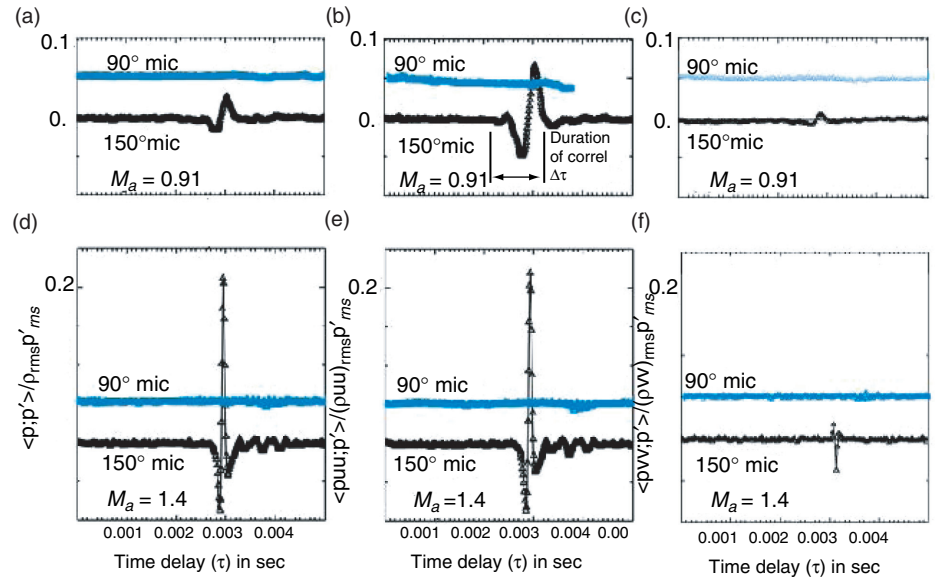


Figure 29: Normalized cross-correlation between sound pressure fluctuations p' and (a), (d) air density ρ ; (b), (e) puu ; (c), (f) pvv fluctuations measured in $Ma = 0.91$ and 1.4 jets. For (a), (b) & (c) laser probe was at $x/D = 10$ & centerline; for (d) & (e) probe is at $x/D = 12$ & centerline; for (f) it is $x/D = 6$ and $r/D = 0.48$. The microphone was kept at $50D$ and at indicated polar angles. The 90° microphone data are shifted by 0.05 . (reprinted from Panda et al. [40], 2005 Cambridge University Press, used with permission).

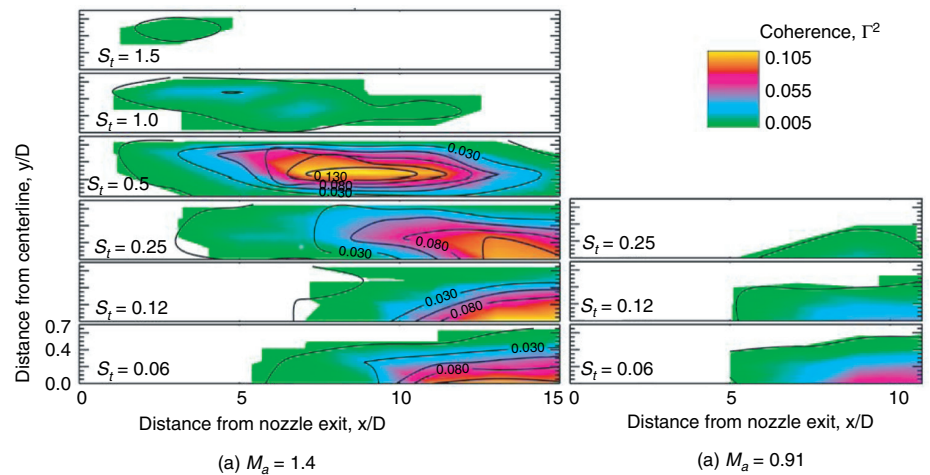


Figure 30: Distribution of normalized cross-spectrum (coherence) between turbulent density fluctuations and far field sound pressure fluctuations at indicated Strouhal frequencies for two different unheated jets. The microphone was fixed at $r/D = 50$, $\theta = 150^\circ$ while the laser probe was moved from point to point. (reprinted from Panda et al. [40]).

that the color scale is such that the minimum value (green for $\Gamma = 0.005$) is above the noise floor ($\Gamma = 0.002$). Therefore regions of no or very low correlation do not show any color. Since no correlation was measured in Mach 0.95 jet for $St \geq 0.4$, coherence distributions at $St = 0.5, 1$ & 1.5 are not plotted. A clear distinction in measurable sound sources in subsonic and supersonic jets is visible in this figure. Density fluctuations causing sound generation up to $St = 1.5$ could be determined only in the supersonic case; the higher the frequency the closer the source to the

nozzle exit. Additionally, the peripheral shear layer around the potential core is found to produce no correlation in the subsonic jet, while significant correlation at high frequency is measured in the Mach wave emitting supersonic jet. The lower frequency source in both jets is the strongest along centerline, after the end of potential core. Such sources weaken rapidly in the radial direction and very slowly in the downstream direction.

Instead of using a single microphone, researchers opted for a phased-array of microphone to overcome the deficiency of the correlation technique. The correlation levels fell below the measurement noise floor for higher Strouhal frequencies $St > 1.5$, in the low subsonic jets, and also for microphone polar angles of 90° and higher. Since a phased array collects sound waves over a large aperture, the expectation was that the beamformed signal would provide improved correlation over that from a single microphone. However, the improvement was found to be small. The data also indicated that in the near field of a jet the propagation speed of the pressure fluctuations was different from that of the ambient sound speed. Figure 31 shows the setup with a 32 channel array of electrets microphones mounted on a semi-cylindrical “bucket” located just below the laser probe volume. The array was concentric with the jet cross-section. It was also traversed with the laser probe volume located at the center of the array. The semi-circular array had a radius of 9.25” and the microphones were arranged in two concentric ellipses. The bulk of the correlation data are from single microphones mounted on a 50D (D: nozzle exit diameter) arc for the unheated jet and 100D for the heated jet facility. The laser probe volume was traversed on an x-r plane (x: axial, r: radial directions) containing the jet centerline.

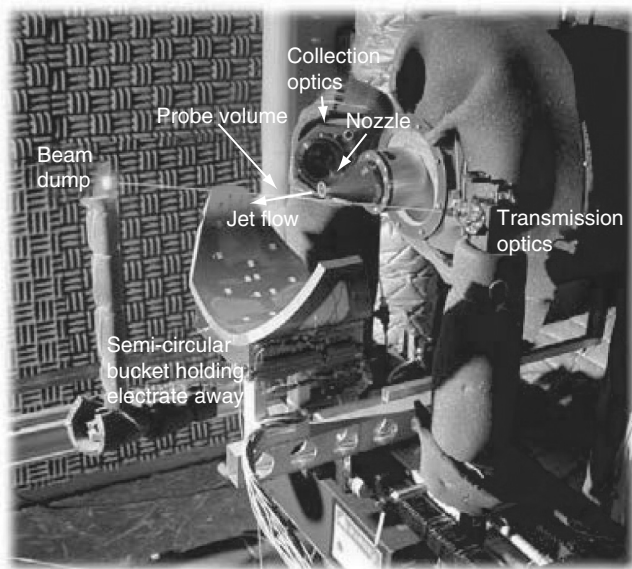


Figure 31: Photograph of the 1 inch NASA Glenn CW-17 small unheated jet facility. (reprinted from Panda et al. [40])

Many of the observations of the correlation study, namely the high correlation values for polar angles close to the jet axis, and the lack thereof at higher polar angles, were in agreement with the two-sources of jet noise that Tam et al elaborated in [50]. All of these have provided boost to the newer trend of separate modeling for high and low frequency parts of the noise sources. Additionally groups at NASA have worked on characterizing jet noise ([51], [52]).

5. HIGHER ORDER SPECTRAL ANALYSIS

5.1. INTRODUCTION

Initially, researchers used Higher-Order Spectral methods were used by researchers in electrical sciences for understanding the non-linearity in electrical systems, resulting in several useful non-linear spectral tools. These tools proved immensely useful in other subjects and were used to understand several other physical phenomena such as glacial dynamics, manufacturing sciences, free shear flows, etc. The extensive role of non-linearity in these systems necessitates the use of non-linear tools for a proper physical understanding.

Higher order spectral analysis was first employed by Ponton and Seiner [53] and by Walker and Thomas [54] to unravel the non-linearity in high speed flows. Ponton and Seiner [53] used an azimuthal array of microphones around a choked circular jet. Time-domain and frequency domain analyses, including non-linear spectral analysis helped identify the helical mode of instability of the jet. These higher-order methods also revealed the random rotation of the jet flapping plane. The auto-bicoherence spectra of the microphone signal helped identify the nonlinear interactions. The experiments of Walker and Thomas [54] on rectangular screeching jets discerned the limitations of conventional spectra and the advantages of non-linear spectra. It was demonstrated that while conventional quantities such as SPL, spectra, coherence are easily brought out by linear spectra, the subtle information such as the non-linear wave interactions can be identified only by non-linear spectral methods.

During the course of research conducted by Srinivasan et al. [55,56] on twin jet coupling problems, they encountered jets that they deemed uncoupled by linear spectral methods but showed large non-linearities evident from Lissajou plots, indicative of some non-linear coupling. Therefore, they resorted to non-linear spectral methods.

5.2. PRINCIPLE

The basic higher-order tools comprise the auto-and cross-bispectra. The auto- and cross-bispectra are the triple correlations of two functions, transformed into the frequency domain by a Fourier transform. The mathematical form of cross-bispectrum is shown in Equation 52:

$$B_{yxx}(f_1, f_2) = \lim_{T \rightarrow \infty} \frac{1}{T} \int_0^T y(t)x(t+\tau_1)x(t+\tau_2) dt \exp\{i2\pi(f_1\tau_1 + f_2\tau_2)\} d\tau_1 d\tau_2 \quad (52)$$

Cross-bicoherence is the normalized cross-bispectrum of the two time series signals acquired simultaneously. To calculate this quantity, the discrete frequency domain form is suitable for computations. The discrete cross-bispectrum is expressed for an ensemble (k) as,

$$S_{YXX}^{(k)}(f_1, f_2) = Y^{(k)}(f_1 + f_2) X^{(k)*}(f_1) X^{(k)*}(f_2) \quad (53)$$

where $X^{(k)}(f)$ and $Y^{(k)}(f)$ are the DFT of discrete time series signals $x(t)$ and $y(t)$. Then, an ensemble average is done over M assemblies to obtain the final estimate of discrete cross-bispectrum.

$$S_{YXX}(f_1, f_2) = \frac{1}{M} \sum_{k=1}^M S_{YXX}^{(k)}(f_1, f_2) \quad (54)$$

The cross-bicoherence spectrum is then obtained by normalizing this quantity with the power spectra of the two signals as follows:

$$b_c^2(f_1, f_2) = \frac{|S_{YXX}(f_1, f_2)|^2}{\frac{1}{M} \sum_{k=1}^M |Y^{(k)}(f_1 + f_2)|^2 \frac{1}{M} \sum_{k=1}^M |X^{(k)}(f_1)X^{(k)}(f_2)|^2} \quad (55)$$

The computation of these quantities is simplified by using symmetry properties in the frequency domain. Below, we discuss practical use of the cross-bispectra, leading to the development of a new bi-spectral metric.

5.3. IMPLEMENTATION

Srinivasan et al. ([55], [56]) performed experiments on two contrasting configurations of bevelled rectangular twin jets; one where the bevels faced each other, (termed as co-directed twin jets) and the other where the bevels faced on opposite sides (called contra-directed twin jets) as shown in Figure 32. The corresponding cross-bicoherence spectra are plotted against the respective geometries in Figure 32. As shown in Figure 32, while the co-directed twin jets possessed several modal interactions, leading to peaks in the cross-bicoherence, the contra-directed jets were relatively free of peaks (and hence, quadratic modal interactions). Based on these interesting observations, they counted the number of peaks in the cross-bispectra, leading to the development of a pertinent metric called interaction density, defined as

$$I_{c,n} = \sum_{i=1}^N \sum_{j=1}^M \mathbb{I}(i, j), \quad \mathbb{I}(i, j) = \begin{cases} 1 & b_c^2(f_i, f_j) \geq n \\ 0 & b_c^2(f_i, f_j) < n \end{cases} \quad (56)$$

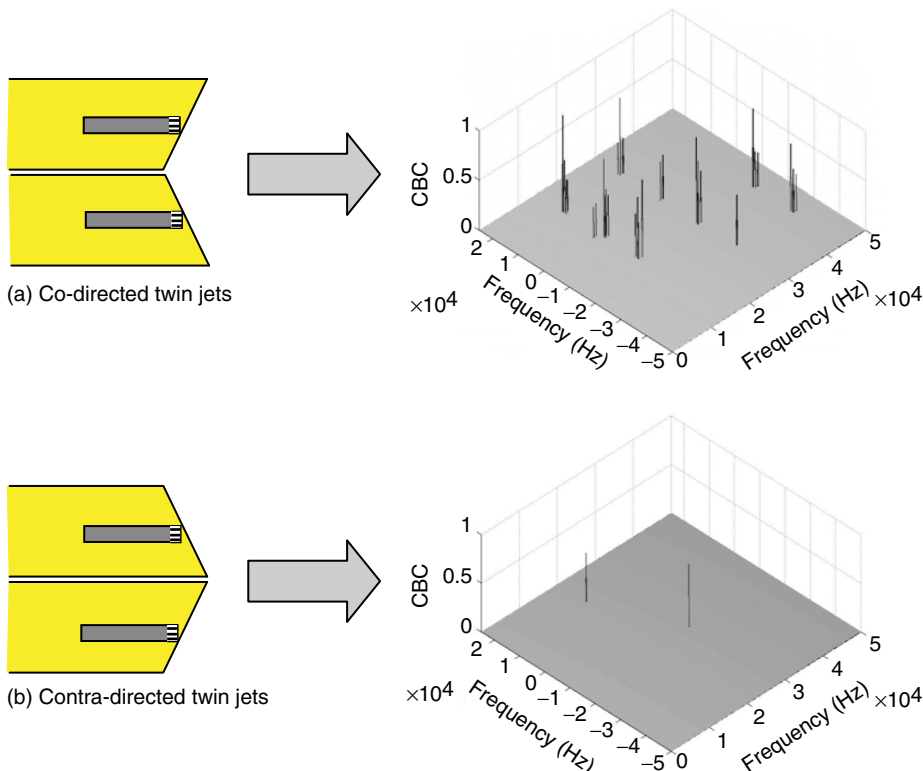


Figure 32: Twin-jets in co-directed and contra-directed configurations and their corresponding cross-bicoherence spectra. (reprinted from Srinivasan et al. [56], 2009 Elsevier Ltd., used with permission).

In summary, the interaction density is the count of the number of quadratic interactions in a bi-spectrum possessing cross-bicoherence values above a certain threshold [n in Eq. (41)]. It was demonstrated that the interaction density metric, when plotted against pertinent flow/geometric parameters, peaks during crucial occurrences such as mode-switches. This concept is exemplified in Figure 33, where the interaction density metric is plotted against the Mach number for co-directed twin beveled rectangular jets. The interaction density shows a peak around Mach number of 1.33, wherein there is a transition from symmetric to anti-symmetric coupling of the twin jets. One may visualize these two coupling modes from the technique explained earlier, using Figure 22.

Srinivasan et al. [56] also explained the formation of closely spaced quadratic interactions, called clusters, due to multiple peaks in the vicinity of each other. Quadratic interactions occur between compatible modes and propagate into a series of interactions, as depicted in Figure 34, leading to the formation of clusters. Thus, the more non-linear interactions, the higher the number of peaks in the bi-spectra, and hence the higher interaction density.

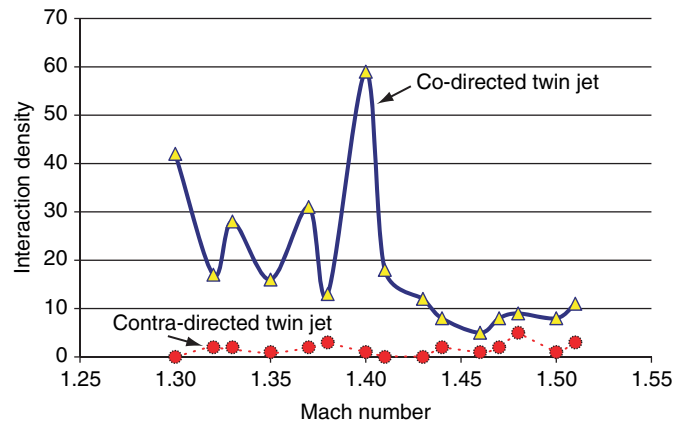


Figure 33: Variation of Interaction Density with Mach number for co-directed and contra-directed twin jets, with threshold value of 0.3. (reprinted from Srinivasan et al. [56], 2009 Elsevier Ltd., used with permission).

Panickar, Srinivasan, and Raman [57] tested the interaction density metric for other situations involving other jets on a variety of combinations: single jets, twin jets, circular geometries, regular rectangular geometries and beveled rectangular geometries. For instance, three different jet instability circumstances are depicted in Figure 35. Figure 35(a) shows a jet from a single beveled nozzle switching from anti-symmetric mode to symmetric mode around Mach 1.4, wherein the interaction density metric sharply increases and levels off to normal values after the mode-switch. Figure 35(b) shows a switch from one oblique mode to another in twin rectangular jets. Here, since the mode switch is not strong as compared to switches from symmetric to anti-symmetric, the rise in interaction density values is not as sharp. Nevertheless, the metric shows its propensity to predict even weak mode-switches. In Figure 35(c), where a circular jet switches from flapping to helical mode and the axisymmetric mode ceases to operate, in both these cases the interaction density shows a sharp rise around the catastrophic regimes. This behavior was attributed to the sudden changes in the energy cascade that can be expected in mode-switching scenarios. Joshi et al. [58] tested the interaction density metric on yawed rectangular jet configurations. They constructed two test cases of rectangular twin jets that were geometrically similar at the exit by considering regular rectangular jets and beveled and yawed rectangular jets as shown in Figure 36.

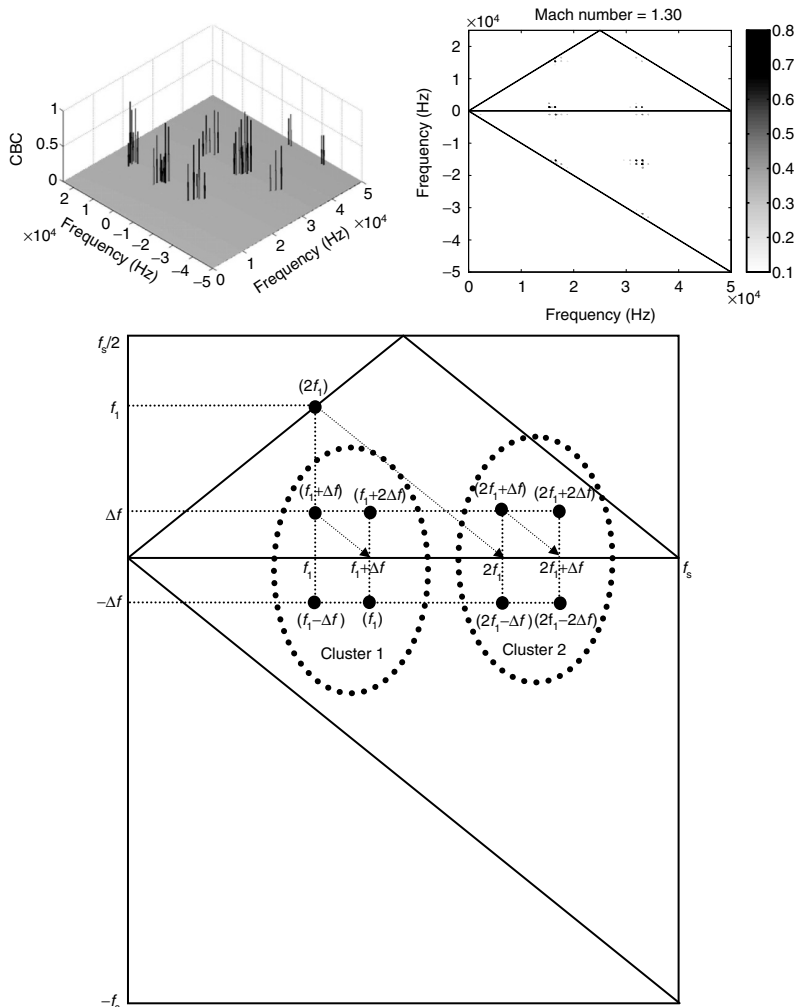


Figure 34: Examples of clustered interactions. Top: Bi-coherence spectra. Bottom: Explanation of clustering. (reprinted from Srinivasan et al. [56], 2009 Elsevier Ltd., used with permission).

Although they are geometrically similar at the jet exit, they are kinematically dissimilar due to the bevel and yaw angles. Although the linear spectra and mode-switches are similar in behavior, the interaction density metric shows a sharp increase in values, distinguishing the beveled and yawed case from the regular rectangular case. Thus, higher order spectral analysis provides deep insights into the flow and acoustic behavior of flow systems. In particular, the cross-bicoherence proves to be a reliable tool for predicting changes and differences in flow and resonance systems. In summary, higher order spectral analyses illuminate phenomena that normally go un-detected by conventional techniques. We can state with confidence that these promising results have merely scratched the surface of this technique's potential.

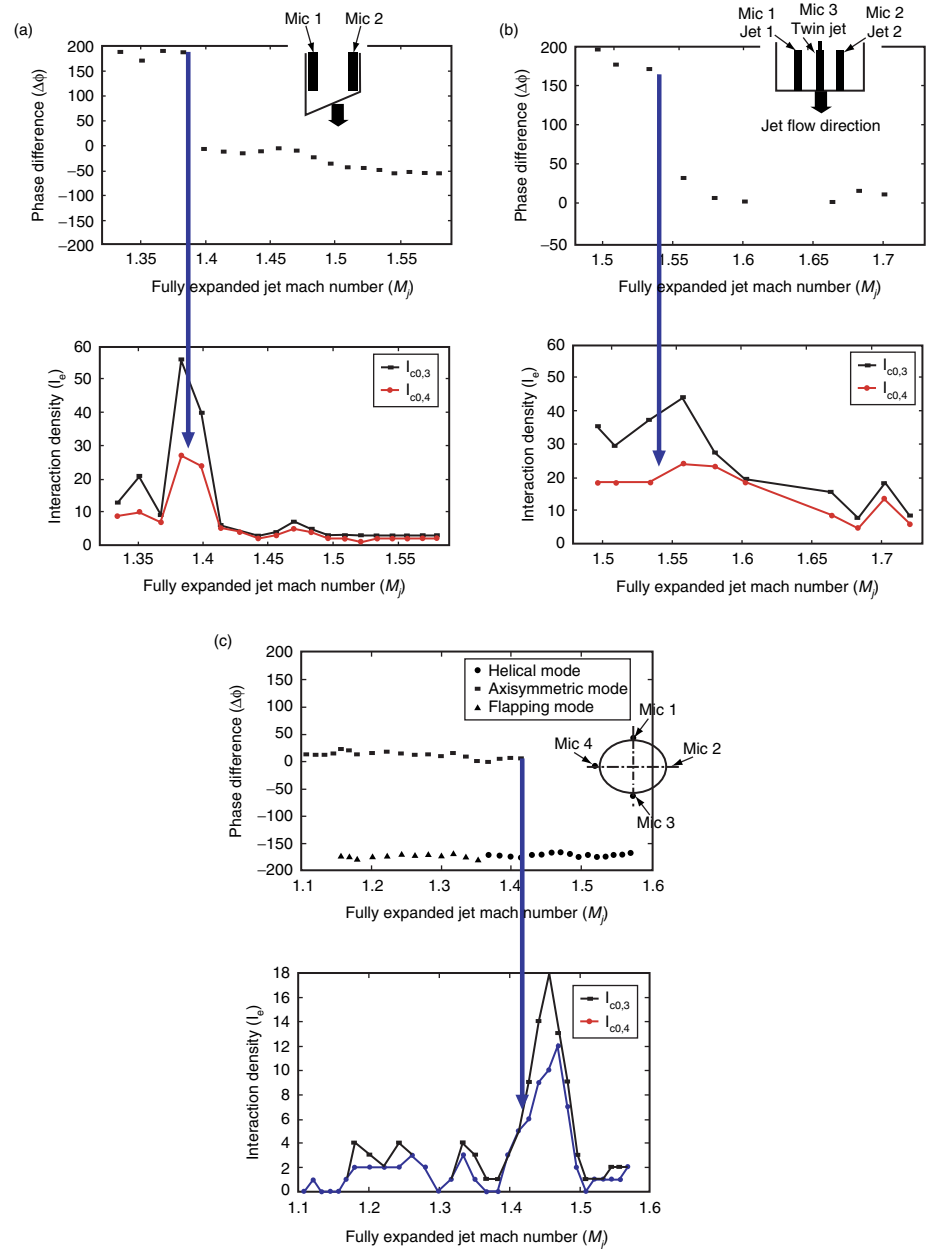


Figure 35: Demonstration of the use of interaction density in predicting mode-switches in jet instability situations. Interaction density peaks around mode-switch conditions in (a) jet from beveled rectangular nozzle, (b) twin jets from twin-rectangular nozzles, and (c) single circular jet. (reprinted from Panickar et al. [57], 2005 American Institute of Physics, used with permission).

6. CONCLUSIONS

This review focuses on five advanced techniques in experimental aeroacoustics that have a tremendous potential as experimental tools in aeroacoustics to address issues such as (i) source location, (ii) noise mechanisms such as resonant oscillations, (iii) instability modes in resonant scenario, and (iv) dynamical issues and catastrophic situations in aeroacoustic problems. Advances in the experimental techniques have enhanced our knowledge of various aeroacoustic noise source mechanisms such as aerodynamic noise from wind turbine blades, flow-structure interaction noise, resonant flow acoustics, etc. Microphone array beamforming and near-field holography will soon become the standard for noise source localization.

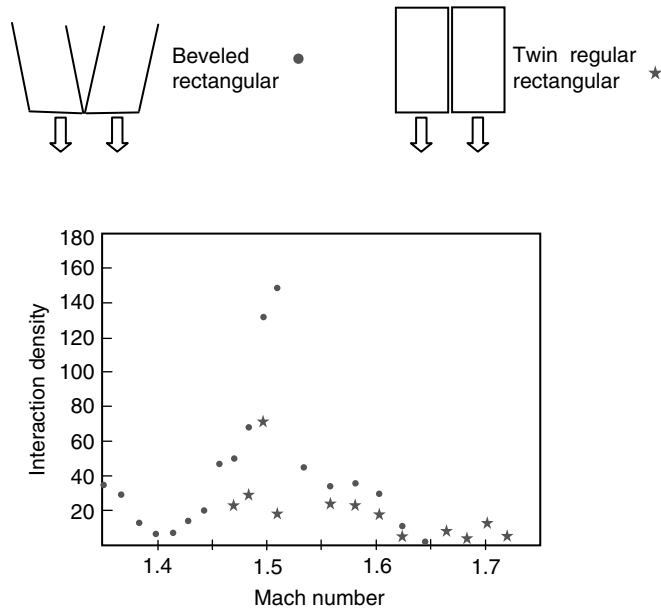


Figure 36: Demonstration of the use of interaction density metric in regular and yawed twin rectangular jets. (reprinted from Joshi et al. [58], 2006 AIAA, used with permission)

Simultaneous flow/acoustic measurements help shed light on the complex mechanisms that generate tonal noise due to resonant flow interactions. High order spectral analysis serves as an important tool to unravel non-linearity in high speed flows. We hope that in addition to being a resource, this review will arouse more interest in experimental aeroacoustics.

ACKNOWLEDGMENTS

The authors are grateful to several individuals who provided insightful comments and gave us permission to include illustrations from their work. This includes Drs. M. Samimy, M. Kearney-Fischer, D. Long, A. Cain, C. Nelson, J. Panda, P. Panickar, S. Sarpotdar and R. Perschke. The source of each figure is noted in the caption with a reference to the original publication.

REFERENCES

- [1] Goldstein, M., "Aeroacoustics," McGraw Hill, New York, 1976.
- [2] Hubbard, H.H. (Ed.), "Aeroacoustics of Flight Vehicles," Acoustical Society of America, Vols. 1 & 2, 1991.
- [3] Mueller, T. J. (Ed.), "Aeroacoustic Measurements," Springer, New York, 2002.
- [4] Turkdogru, N., and Ahuja, K. K., "Determination of geometric farfield for ducted and unducted rotors.", International Journal of Aeroacoustics, Vol. 11(5), pp. 607–628, 2012.
- [5] Vishwanathan, K., and Clark, L. T., "Effect of nozzle contour on jet aeroacoustics", International Journal of Aeroacoustics, Vol. 3(2), pp. 103–135, 2004.
- [6] Billingsley, J. and Kinns, R., "The Acoustic Telescope", J. Sound Vib., Vol. 48, pp. 485–510, 1976.

- [7] Boone, M. M., Kinning, N. and van den Dool, T., "Two-dimensional noise source imaging with a T-shaped microphone cross array", *J. Acoust. Soc. Am.*, Vol. 108(6), pp. 2884–2890, 2000.
- [8] Dougherty, R. P. and Stoker, R.W., "Sidelobe suppression for phased array aeroacoustic measurements", AIAA-1998-2242, 1998.
- [9] Brooks, T. F. and Humphreys, Jr, W. M., "A Deconvolution Approach for the Mapping of Acoustic Sources (DAMAS) determined from phased microphone array," *J. Sound Vib.*, Vol. 294(4–5), pp. 856–879, July 2006.
- [10] Dougherty, R. P., "Extensions of DAMAS and Benefits and Limitations of Deconvolution in Beamforming", AIAA-2005-2961, 2005.
- [11] Sijtsma, P., "CLEAN based on spatial source coherence", *Int. J. Aeroacoustics*, Vol. 6, pp. 357–374, 2007.
- [12] Dougherty, R. P., "Advanced Time-domain Beamforming Techniques", AIAA-2004-2955, 2004.
- [13] Dougherty, R. P. and Podboy, G., "Improved Phased Array Imaging of a Model Jet," AIAA-2009-3186, 2009.
- [14] Sarradj, E., "A fast signal subspace approach for the determination of absolute levels from phased microphone array measurements", *J. Sound Vib.*, Vol. 329(9), pp. 1553–1569, April, 2010.
- [15] Brusniak, L., "DAMAS2 Validation for flight test airframe noise measurements," Berlin Beamforming Conference (BeBec), 2008.
- [16] Ehrenfried, K., and L. Koop, "A Comparison of Iterative Deconvolution Algorithms for the Mapping of Acoustic Sources," AIAA-2006-2711, 2006.
- [17] Schmidt, O., "Multiple emitter location and signal parameter estimation," in *Proc. RADC Spectrum Estimation Workshop*, pp. 243–258, Oct. 1979.
- [18] Suzuki, T., "Generalized inverse beam-forming algorithm resolving coherent/ incoherent, distributed and multipole sources," AIAA-2008-2954, 2008.
- [19] Dougherty, R., P., "Improved generalized inverse beamforming for jet noise," *International Journal of Aeroacoustics*, Vol. 11 (3, 4), pp. 259–289, 2012.
- [20] Nelson, C. C., Cain, A. B., Dougherty, R., Brentner, K. S. and Morris, P. J., 2013, "Application of Synthetic Phased Array Techniques to Hot Supersonic Jet Noise," AIAA-2013-0327, 2013.
- [21] Panickar, P., Erwin, J. P., Sinha, N., Murray, N. E. and Lyons, G., "Localization of Acoustic Sources in Shock-Containing Jet Flows Using Phased Array Measurements," AIAA-2013-0613, 2013.
- [22] Ramachandran, R. C. and Raman, G., "Evaluation of Various Beamforming Algorithms for Wind Turbine Noise Measurement," AIAA-2011-2388, 2011.
- [23] Ramachandran, R. C., Raman, G. and Dougherty, R. P., "Noise Source Localization Using a Compact Phased Array: Studies on a Full Scale Wind Turbine in a Wind," *Wind Engineering*, Vol. 36(5), pp. 589–604, 2012.

- [24]Wagner, S., Bareiss, R. and Guidati, G., *Wind Turbine Noise*, Springer, Berlin, 1996.
- [25]Oerlemans, S., Sijtsma, P. and Mendez Lopez, B., "Location and quantification of noise sources on a wind turbine," *Journal of Sound and Vibration*, Vol. 299, pp. 869–883, 2007.
- [26]Brooks, T. F., Pope, G. S. and A., M. M., "Airfoil Self Noise and Prediction," NASA Reference publication 1218, 1989.
- [27]Dougherty, R. P., Ramachandran, R. C. and Raman, G., "Deconvolution of Sources in Aeroacoustic Images from Phased Microphone Arrays Using Linear Programming", AIAA-2013-2210, June 2013.
- [28]Ramachandran, R. C., Raman, G., and Dougherty, R. P., "Linear Programming Acoustic Beamforming Versus Other Deconvolution Methods For A Full Scale 1.5 MW Wind Turbine.", AIAA-2013-2057, June 2013.
- [29]Perschke, R., Ramachandran, R. C., and Raman, G., "Detection of Flow Separation Using Microphone Arrays," *BeBeC 2012-19*, 4th Berlin Beamforming Conference, February, 2012.
- [30]Howe, M. S., " A Review of the Theory of Trailing Edge Noise", *Journal of Sound and Vibration*, Vol. 61, pp. 437–465, 1978.
- [31]Lighthill, M. J., "On sound generated aerodynamically I. General Theory", *Proc. R. Soc. A*, Vol. 211, pp. 564–587, 1952.
- [32]Curle, N., "The influence of solid boundaries upon aerodynamic sound", *Proc. R. Soc. A*, Vol. 231, pp. 504–514, 1955.
- [33]Maynard, J. D., Williams, E. G., and Lee, Y., "Nearfield Acoustic Holography: I. Theory of Generalized Holography and the Development of NAH", *The Journal of Acoustical Society of America*, Vol. 78, pp. 1395, 1985.
- [34]Williams, E. G., Dardy, H. D., and Washburn, K. B., "Generalized Nearfield Acoustical Holography for cylindrical geometry: Theory and Experiment", *The Journal of Acoustical Society of America*, Vol. 81, pp. 389, 1987.
- [35]Valdivia, N. and Williams, E. G., "Implicit Methods of Solution to Integral Formulations in Boundary Element Method Based Nearfield Acoustic Holography", *The Journal of Acoustical Society of America*, Vol. 116, pp. 1559, 2004.
- [36]Valdivia, N. P. and Williams, E. G., "Study of the Comparison of the Methods of Equivalent Sources and Boundary Element Methods for Near-field Acoustic Holography", *The Journal of Acoustical Society of America*, Vol. 120, pp. 3694, 2006.
- [37]Long, D. and Martens S., "Simultaneous Noise and Performance Measurements for High Speed Jet Noise Reduction Technologies," *ASME GT2009- 59073*, June 2009.
- [38]Panickar, P., Srinivasan, K. and Raman, G., "Aeroacoustic features of coupled twin jets with spanwise oblique shock-cells.", *Journal of Sound and Vibration*, Vol. 278, pp. 155–179, 2004.
- [39]Sarpotdar, S., Raman, G., and Cain, A. B., "Powered resonance tubes: resonance characteristics and actuation signal directivity.", *Experiments in Fluids*, Vol. 39(6), pp.1084–1095, 2005.

- [40]Panda, J., "Identification of noise sources in high speed jets via correlation measurements – A Review.", AIAA-2005-2844, May 2005.
- [41]Panda, J., "Experimental investigation of turbulent density fluctuation and noise generation from heated jets.", *Journal of Fluid Mechanics*, Vol. 591, pp. 73–96, 2007.
- [42]Panda, J., and Seaholtz, R. G., "Experimental investigation of density fluctuations in high-speed jets and correlation with generated noise.", *Journal of Fluid Mechanics*, Vol. 450, pp. 97–130, 2002.
- [43]Panda, J., Seaholtz, R. G., and Elam, K. A., "Investigation of noise in high-speed jets via correlation measurements.", *Journal of Fluid Mechanics*, Vol. 537, pp. 349–385, 2005.
- [44]Hileman, J. I., Thurow, B. S., Caraballo, E. J., and Samimy, M., "Large-scale structure evolution and sound emission in high-speed jets: real-time visualization with simultaneous acoustic measurements.", *Journal of Fluid Mechanics*, Vol. 544(1), pp. 277–307, 2005.
- [45]Hileman, J., and Samimy, M., "Turbulence structures and the acoustic far field of a Mach 1.3 jet.", *AIAA journal*, Vol. 39(9), pp. 1716–1727, 2001.
- [46]Hileman, J., Thurow, B., and Samimy, M., "Exploring noise sources using simultaneous acoustic measurements and real-time flow visualizations in jets.", *AIAA journal*, Vol. 40(12), pp. 2382–239, 2001.
- [47]Kearney-Fischer, M., Sinha, A., and Samimy, M., "Intermittent nature of subsonic jet noise.", *AIAA Journal*, Vol. 51, pp. 1142–1155, 2013.
- [48]Kearney-Fischer, M., Kim, J. H., and Samimy, M., "A study of Mach wave radiation using active control.", *Journal of Fluid Mechanics*, Vol. 681, pp. 261–292, 2011.
- [49]Sinha, A., Alkandry, H., Kearney-Fischer, M., Samimy, M., and Colonius, T., "The impulse response of a high-speed jet forced with localized arc filament plasma actuators," *Physics of Fluids*, Vol. 24, 125104, 2012.
- [50]Tam, C. K., Viswanathan, K., Ahuja, K. K., and Panda, J., "The Sources of Jet Noise: Experimental Evidence," AIAA-2007-3461, 2007.
- [51]Bridges, J., and Wernet, M., "Measurements of the Aeroacoustic Sound Source in Hot Jets", AIAA-2003-3130, 2003.
- [52]Seiner, J.M., Ukeiley, L.S., Ponton, M.K., and Jansen, B.J., "Progress in experimental measure of turbulent flow for aeroacoustics," AIAA 2002-2402, 2002.
- [53]Walker, S.H. and Thomas, F.O., "Experiments characterizing nonlinear shear layer dynamics in a supersonic rectangular jet undergoing screech", *Physics of Fluids*, Vol. 9, pp. 2562–2579, 1997.
- [54]Ponton, M.K. and Seiner, J.M., "Acoustic study of B helical mode for choked axisymmetric nozzle", *AIAA Journal*, Vol. 33, pp. 413–420, 1995.
- [55]Srinivasan, K. , Panickar, P., Raman, G., Kim, B-H., and Williams, D., "Study of Supersonic Twin Jet Coupling Using Higher Order Spectral Analysis", AIAA-2003–3871, June 2003.
- [56]Srinivasan, K., Panickar, P., Raman, G., Kim, B. and D. Williams, "Study of coupled supersonic twin jets of complex geometry using higher order spectral analysis", *Journal of Sound and Vibration*, Vol.

323(3-5), pp. 910-931, June 2009.

- [57]Panickar, P., Srinivasan, K. and Raman, G., "Nonlinear interactions as precursors to mode jumps in resonant acoustics.", *Physics of Fluids*, Vol. 17, pp. 096103.01-096103.18, 2005.
- [58]Joshi, R., Panickar, P., Srinivasan, K. and G. Raman, "Nozzle Orientation Effects and Non-Linear Interactions between Twin Jets of Complex Geometry", *AIAA Journal of Aircraft*, Vol. 43(2), pp. 336-345, 2006.
- [59]Raman, G., Prakash, M., Ramachandran, R. C., Patel, H. and Chelliah, K., "Remote detection of building air infiltration using a compact microphone array and advanced beamforming methods", *BeBeC 2014-14*, (to appear) 5th Berlin Beamforming Conference, February 2014.

EAR PLUGS FOR SPORTS FANS?

Spectators at professional sports games like the Super Bowl need to protect their ears while enjoying the match according to a Canadian expert. "Each time your ears have been ringing, that is evidence of hearing loss. There's no recovery mechanism in place for the death of those inner ear cells," said Dr. Tim Rindlisbacher, director of sports health at Cleveland Clinic in Toronto, where he also works with the CFL's Toronto Argonauts and Mississauga Steelheads of the Ontario Hockey League. Rindlisbacher suggests that season tickets holders over a long period of time could be at considerable risk of noise-induced hearing loss from noisemakers, blaring music and cheering, especially if they also listen to loud music regularly or are exposed to noise at work. "Hearing protection would be a really smart idea," Rindlisbacher said.

VIGILANTES AGAINST NOISE

Washington DC's Dupont Circle neighborhood may no longer be the epicenter of cool, but according to at least one local group, the area's club-goers are still very noisy. The D.C. Noise Control Act limits noise levels at night to 60 decibels and the newly formed D.C. Nightlife Noise Coalition says the volume emanating from some nearby nightlife establishments is disrupting residents' quality of life, and city officials are not enforcing the law. "We finally decided that we need to band together, raise awareness, get the press together, and shine a light on this issue," says Sarah Peck, a lawyer and the coalition's spokeswoman, who wrote a 23-page white paper detailing how the noise ordinances are not being enforced. "We need to take this seriously. This is a few blocks from the White House, and our officials are not taking this seriously." Peck says the coalition largely comprises residents in the Palladium Condominium at 1325 18th St. NW, where she has lived since 2011. The group also has the support of Steve Coniglio, the developer of a 70-unit condominium next to the Tabard Inn on N Street NW, which is in "earshot" to the area south of Dupont Circle along Connecticut Avenue nicknamed Club Central. Together, they have many tactics for fighting noise, including going around at night with a Department of Consumer and Regulatory Affairs-approved sound meter to measure the rowdiness of area establishments. The group is also meeting with government officials to demand they enforce these laws and is protesting at the re-licensing of the worst noise offenders by the Alcoholic Beverage Regulation Administration.